



Mapping intertidal macrophytes in fjords in Southwest Greenland using Sentinel-2 imagery

Carlson, Daniel F.; Vivó-Pons, Antoni; Treier, Urs A.; Mätzler, Eva; Meire, Lorenz; Sejr, Mikael; Krause-Jensen, Dorte

Published in:
Science of the Total Environment

Link to article, DOI:
[10.1016/j.scitotenv.2022.161213](https://doi.org/10.1016/j.scitotenv.2022.161213)

Publication date:
2023

Document Version
Publisher's PDF, also known as Version of record

[Link back to DTU Orbit](#)

Citation (APA):
Carlson, D. F., Vivó-Pons, A., Treier, U. A., Mätzler, E., Meire, L., Sejr, M., & Krause-Jensen, D. (2023). Mapping intertidal macrophytes in fjords in Southwest Greenland using Sentinel-2 imagery. *Science of the Total Environment*, 865, Article 161213. <https://doi.org/10.1016/j.scitotenv.2022.161213>

General rights

Copyright and moral rights for the publications made accessible in the public portal are retained by the authors and/or other copyright owners and it is a condition of accessing publications that users recognise and abide by the legal requirements associated with these rights.

- Users may download and print one copy of any publication from the public portal for the purpose of private study or research.
- You may not further distribute the material or use it for any profit-making activity or commercial gain
- You may freely distribute the URL identifying the publication in the public portal

If you believe that this document breaches copyright please contact us providing details, and we will remove access to the work immediately and investigate your claim.



Mapping intertidal macrophytes in fjords in Southwest Greenland using Sentinel-2 imagery

Daniel F. Carlson^{a,*}, Antoni Vivó-Pons^{a,b}, Urs A. Treier^c, Eva Mätzler^d, Lorenz Meire^{e,f}, Mikael Sejr^{a,g}, Dorte Krause-Jensen^{a,g}

^a Arctic Research Centre, Aarhus University, Ole Worms Allé 1, Aarhus 8000, Denmark

^b Centre for Ocean Life, National Institute of Aquatic Resources, Technical University of Denmark, Kemitorvet, Lyngby 2800, Denmark

^c Department of Biology, Ecoinformatics and Biodiversity, Aarhus University, Ny Munkegade 116, Aarhus 8000, Denmark

^d Government of Greenland, Nuuk, Greenland

^e Greenland Climate Research Centre, Greenland Institute of Natural Resources, Kivioq 2, Nuuk 3900, Greenland

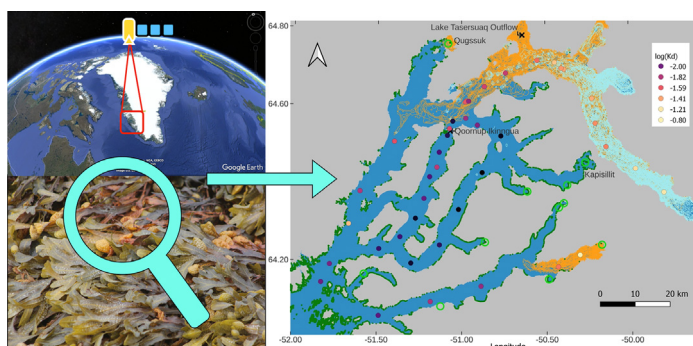
^f Department of Estuarine and Delta Systems, Royal Netherlands Institute for Sea Research, Yerseke, the Netherlands

^g Department of Ecoscience, Marine Ecology, Aarhus University, C.F. Møllers Allé, Building 1131, 8000 Aarhus C, Denmark

HIGHLIGHTS

- Intertidal macrophytes and detached, floating macroalgae were mapped using Sentinel-2 imagery in SW Greenland
- Icebergs and exposed bare bottoms resulted in false positives in the EVI and the FAI
- The spectra of exposed bare bottoms, icebergs, and macrophytes resulted in misclassifications by spectral mixture analysis
- The normalized difference vegetation index (NDVI) produced the most reliable results
- The spatial distribution of intertidal macrophytes appears to be related to icebergs and turbid plumes

GRAPHICAL ABSTRACT



ARTICLE INFO

Editor: Martin Drews

Keywords:

Blue carbon
Macroalgae
Greenland
Remote sensing
Sentinel-2
Vegetation index

ABSTRACT

Changes in the distribution of coastal macrophytes in Greenland, and elsewhere in the Arctic are difficult to quantify as the region remains challenging to access and monitor. Satellite imagery, in particular Sentinel-2 (S2), may enable large-scale monitoring of coastal areas in Greenland but its use is impacted by the optically complex environments and the scarcity of supporting data in the region. Additionally, the canopies of the dominant macrophyte species in Greenland do not extend to the sea surface, limiting the use of indices that exploit the reflection of near-infrared radiation by vegetation due to its absorption by seawater. Three hypotheses are tested: I) 10-m S2 imagery and commonly used detection methods can identify intertidal macrophytes that are exposed at low tide in an optically complex fjord system in Greenland impacted by marine and land terminating glaciers; II) detached and floating macrophytes accumulate in patches that are sufficiently large to be detected by 10-m S2 images; III) iceberg scour and/or turbid meltwater runoff shape the spatial distribution of intertidal macroalgae in fjord systems with marine-terminating glaciers. The NDVI produced the best results in optically complex fjord systems in Greenland. 12 km² of exposed intertidal macrophytes were identified in the study area at low tide. Floating mats of macrophytes ranged in area from 400 m² to 326,800 m² and were most common at the mouth of the fjord. Icebergs and turbidity appear to play a role in structuring the distribution of intertidal macrophytes and the retreat of marine terminating glaciers could allow macrophytes cover to expand. The challenges and solutions presented here apply to most fjords in Greenland and, therefore, the methodology may be extended to produce a Greenland-wide estimate of intertidal macrophytes.

* Corresponding author at: Optical Oceanography, Institute of Carbon Cycles, Helmholtz-Zentrum Hereon, Geesthacht 21502, Germany.
E-mail address: danfcarlson@gmail.com (D.F. Carlson).

1. Introduction

Macroalgae and seagrass, hereafter collectively referred to as ‘macrophytes’, are primary producers that provide numerous ecosystem functions and services in coastal areas (Duffy et al., 2019; Rossiter et al., 2019). Macrophytes stimulate biodiversity and secondary production, affect nutrient cycling (Smale et al., 2013) and contribute to marine carbon sequestration (Blue Carbon; Bayley et al., 2021; Krause-Jensen and Duarte, 2016). Seagrass meadows can sequester carbon locally (Johannessen, 2022) and detached macroalgae can be transported to deep, offshore sinks by ocean currents (Krause-Jensen and Duarte, 2016). Human activities and climate change threaten macrophytes and the ecosystem services that they provide (Duffy et al., 2019), motivating the need for large scale mapping and monitoring tools to quantify current extent and changes.

The impacts of climate change on macrophytes are acutely felt in the Arctic (Filbee-Dexter et al., 2019; Krause-Jensen et al., 2020; Marbà et al., 2018), where the current warming trend exceeds the global average by a factor of four (Rantanen et al., 2022). Arctic warming may be driving the expansion of macrophytes (Krause-Jensen et al., 2020; Marbà et al., 2017, 2018) but a lack of baseline data, as well as the methods to produce such a large-scale baseline, makes quantifying any changes difficult. Arctic macrophytes may also make significant contributions to Blue Carbon (Krause-Jensen and Duarte, 2014), further necessitating the development of large-scale monitoring tools.

Greenland is of particular interest, as it is the world's largest island with an extensive, rocky coastline (Loring and Asmund, 1996) that provides suitable substrate for macroalgae (Krause-Jensen and Duarte, 2014). Eelgrass (*Zostera marina*) is also found in soft-bottom substrates in the southwest part of the country (Olesen et al., 2015). Coastal macrophytes in Greenland may contribute to carbon sinks, either in fjords, which are characterized by high sedimentation rates (Cottier et al., 2010), or through advection by ocean currents to the deep ocean. Small-scale, *in situ* observations of macrophytes have been carried out in Greenland (Høgslund et al., 2014; Krause-Jensen et al., 2012; Krause-Jensen et al., 2019; Olesen et al., 2015; Schoenrock et al., 2018; Sejr et al., 2021; Thyrring et al., 2021) but the remote locations, limited infrastructure, and harsh weather conditions make field surveys costly, time-consuming, and difficult to scale up to monitor large areas. Large-scale mapping and monitoring capabilities, therefore, are essential, especially when planning where and how to protect coastal ecosystems in Greenland against extraction of resources, as such pressures are increasing as these areas become accessible (Tejsner, 2017).

Monitoring tools that can detect both shallow, coastal macrophyte assemblages and detached, buoyant canopies are urgently needed. Greenland's bathymetry and shallow benthic habitats, however, remain poorly mapped. In addition to the general lack of data on the distribution of coastal macrophytes, pro-glacial marine ecosystems are changing rapidly in response to accelerated mass loss from the Greenland Ice Sheet (Hopwood et al., 2020; Mouginot et al., 2019; Straneo et al., 2022). The elimination of iceberg scour, which will occur when marine-terminating glaciers retreat onto land, may open up additional macrophyte habitats in Greenland's extensive fjord systems. A versatile monitoring system that can quantify concurrent variability in baseline macrophyte distributions as well as changes in iceberg concentrations and light availability will greatly aid in research and management efforts in a rapidly changing Arctic.

Satellite remote sensing has proven useful in large-scale monitoring of coastal macrophytes (Duffy et al., 2019; Schroeder et al., 2019), icebergs (Sulak et al., 2017; Scheick et al., 2019), and turbidity (Klein et al., 2021; Schild et al., 2017). The Landsat archive, which extends to 1982, allows long-term trends to be quantified (Bell et al., 2020; Finger et al., 2021; Hamilton et al., 2020; Lebrasse et al., 2022; Lõugas et al., 2020) but the 30 m spatial resolution limits detection to larger macrophyte patches and may not resolve those growing near the shoreline (Nijland et al., 2019). The revisit time of 16 days also limits the number of available images.

The launch of the Sentinel 2A and 2B satellites in 2015 and 2017, respectively, (Main-Knorn et al., 2017) provides improved spatial and temporal resolution, enhancing monitoring capabilities for coastal

macrophytes. The Multi-Spectral Instrument (MSI) onboard the Sentinel-2 (S2) satellites provides data in 13 spectral bands from the visible to the short-wave infrared portions of the spectrum at spatial resolutions of 10–60 m (Main-Knorn et al., 2017). The S2-MSI satellites have a revisit time of 5 days at the equator and 2–3 days above 45° (Drusch et al., 2012). The 10 m spatial resolution in the blue, green, red, and near-infrared bands permits the detection of smaller macrophyte beds when compared to Landsat (Zoffoli et al., 2020). The planned launches of two additional, identical satellites will maintain S2-MSI data coverage until 2030 (Pahlevan et al., 2017), enabling monitoring of coastal macrophytes at seasonal, interannual, and decadal time scales (Wilson et al., 2020).

The recent availability of 10 m S2-MSI imagery, concurrent developments in open source atmospheric correction and analysis software, and the proliferation of small unoccupied aerial systems (UAS; Johnston, 2019; Joyce et al., 2019; Rossiter et al., 2019) have led to a similar and largely reproducible workflow (Pottier et al., 2021). In general, this workflow often uses ACOLITE (Vanhellemont, 2019) to perform atmospheric correction of S2-MSI imagery, which is then analyzed for coastal macrophytes using open source software like Quantum GIS (QGIS) and Sentinel Application Platform (SNAP). The very-high-resolution imagery acquired by UAS has proven useful in training data for classifiers and for cross-validation of macrophytes that are detected in the coarser resolution satellite imagery (Carpenter et al., 2022; Huovinen et al., 2020; Sotille et al., 2020; St-Pierre and Gagnon, 2020). The use of UAS has also benefited from the development of standardized protocols for coastal image processing (Over et al., 2021).

The detection of macrophytes in satellite imagery depends largely on the depth and position of the canopy in the water column. Vegetation reflects strongly in the NIR wavelengths while seawater has low reflectance in the visible wavelengths and absorbs NIR radiation (Jensen, 1980; Schroeder et al., 2019). The difference in NIR reflectance/absorbance can allow exposed/emerged macrophytes to be distinguished from the surrounding seawater (Bell et al., 2020; Cavanaugh et al., 2021; Finger et al., 2021; Hamilton et al., 2020; Huovinen et al., 2020; Jensen, 1980; Schroeder et al., 2019). Different detection methods, therefore are employed for floating canopies, exposed intertidal macrophytes, and submerged, subtidal vegetation. Variations in depth, optically active substances in the water, and location-specific factors like solar zenith angle, ice, and tides, can also influence the type macrophyte detection method used.

Subtidal macrophyte detection is, perhaps, most challenging, as it requires additional data to identify optically shallow waters and to correct for light attenuation by optically active substances in the overlying water column (Kuhwald et al., 2021; Kutser et al., 2020). Bathymetry data, therefore, play an important role in subtidal benthic classifications of remote sensing data. Bathymetry data are used to mask out optically deep water and to verify the satellite retrievals of bathymetry. In addition to bathymetry data, *in situ* observations of optical water properties can aid in the water column corrections required to estimate bottom reflectance (Kuhwald et al., 2021). Subtidal benthic classifications also require accurate atmospheric correction as the reflected radiation signal is weaker due to attenuation by the water column (Kutser et al., 2020). *In situ* reflectance measurements, therefore, are helpful in verifying the results of the atmospheric correction algorithm used.

The use of S2-MSI imagery to detect coastal macrophytes has extended from clear tropical waters to increasingly optically complex waters in temperate and high latitudes (Huovinen et al., 2020; Kotta et al., 2018; Kuhwald et al., 2021; Légaré et al., 2022; Mora-Soto et al., 2020; Wilson et al., 2020). Greenland-specific satellite mapping and monitoring tools for coastal macrophytes, however, have yet to be developed. The lack of such tools is likely due to the lack of supporting data and the complexity introduced by large spatiotemporal gradients in optical properties. Optical gradients are driven by the complex and dynamic fluxes at the interfaces between terrestrial, freshwater, and marine systems and also by exchange processes between fjords and shelf seas. Fjord systems that contain marine-terminating glaciers are especially challenging due to the co-

occurrence of icebergs and sediment-laden freshwater runoff, which are spectrally similar (Hodgkins et al., 2016).

In addition to the large and dynamic optical gradients in Greenland's glaciated fjord systems, the detection of macrophytes in S2-MSI imagery is complicated by limited bathymetry data and macrophyte morphology. The best available Greenland-wide bathymetry data have a coarse resolution of 150 m (Bed Machine, Morlighem et al., 2017) that do not resolve, for example, skerry islands and jagged coastlines, which are prime macroalgae habitats. As a result, the available bathymetry data are not sufficient for estimating bottom reflectance or for masking deep water. The eelgrass meadows and the macroalgal beds do not produce canopies that float on the sea surface. The lack of floating canopies therefore, further complicates macrophyte detection in S2-MSI imagery in Greenland's fjord systems. Other complicating factors include large variations in solar zenith angle, topographic shading, seasonal sea ice cover, large semi-diurnal tidal range, clouds, and fog.

This paper addresses the challenges posed by the unique combination of data limitations, macrophyte morphology and optical complexity in Greenland's fjord systems by applying established vegetation detection methods to S2-MSI imagery of Nuup Kangerlua (NK) and Ameralik (Fig. 1A). These fjords were selected because they are some of the largest and best-studied in Greenland. The lack of high-resolution bathymetry data was circumvented by detecting intertidal macrophytes that were exposed at low tide. The distributions of macrophytes that were identified in S2-MSI imagery were cross-validated using very high resolution aerial imagery that was acquired by UAS (Fig. 1B). Historical *in situ* data produced by past projects, as well as limited data from ongoing monitoring programs, was compiled to validate classifications of macrophytes and S2-derived turbidity.

Intertidal macrophyte detection in NK and Ameralik is attempted using methods that were previously demonstrated in temperate and/or high-latitude coasts (Nijland et al., 2019) and glacier-impacted fjords (Huovinen et al., 2020). These methods include the normalized difference vegetation index (NDVI; Rouse et al., 1974), the enhanced vegetation index (EVI; Huete and Justice, 1999), the floating algae index (Hu, 2009), and spectral mixture analysis. The NDVI is commonly used to identify vegetation in remote sensing data. The NDVI uses the normalized difference in reflectance between the NIR and red bands and is defined as.

$$NDVI = (R_{NIR} - R_{red}) / (R_{NIR} + R_{red}) \quad (1)$$

where R denotes the reflectance and the subscripts indicate the near-infrared (NIR) and red wavelengths.

Thus, a positively sloping reflectance curve between the red and the NIR will result in a positive NDVI, which can be used to identify vegetated pixels. The NDVI has been used to detect floating kelp canopies (Huovinen et al., 2020; Mora-Soto et al., 2020; Nijland et al., 2019; Schroeder et al., 2019) and intertidal macrophytes (Carpenter et al., 2022; Légaré et al., 2022; O'Neill and Costa, 2013; Taddia et al., 2020; Wilson et al., 2020; Zoffoli et al., 2020).

The EVI modifies the NDVI by including gain coefficients and reflectance in the blue band and is defined as.

$$EVI = 2.5 * (R_{NIR} - R_{red}) / (R_{NIR} + 6 * R_{red} - 7.5 * R_{blue} + 1) \quad (2)$$

The EVI has been applied to the monitoring of green tide blooms (Xiao et al., 2019) and floating kelp canopies (Huovinen et al., 2020).

The FAI identifies floating algae using the difference between the red edge reflectance and a linear baseline between the red and the short-wave infrared (SWIR) bands and is defined as.

$$FAI = R_{rcNIR} - R'_{rcNIR} \\ \text{where } R'_{rcNIR} = R_{RCred} + (R_{RCswir} - R_{RCred}) * (\lambda_{NIR} - \lambda_{red}) / (\lambda_{SWIR} - \lambda_{red}) \quad (3)$$

and λ corresponds to the wavelength.

The FAI has been used to identify floating mats of *Sargassum* (Wang et al., 2019) and to detect floating kelp canopies (Huovinen et al., 2020; Mora-Soto et al., 2020).

Spectral mixture analysis (SMA) uses spectral end-members to represent multiple sources of reflectance (e.g., kelp, sand, water) in a linear mixture model that estimates the relative abundance of end-members in each pixel (Keshava, 2003). SMA may be useful when smaller macrophyte beds cannot be resolved by the spatial resolution of the satellite sensor, resulting in a mixture of reflectances from multiple sources in a single pixel (Schroeder et al., 2019). SMA, therefore, provides sub-pixel estimates of end-member abundances, as long as those end-members are spectrally distinct (Keshava, 2003). The efficacy of SMA drops when two or more end-members exhibit similar spectral properties. SMA has been used to detect floating kelp canopies (Bell et al., 2015; Cavanaugh et al., 2011; Huovinen et al., 2020; Friedlander et al., 2018; Schroeder et al., 2019).

The ability of the NDVI, EVI, FAI, and SMA to identify intertidal macrophytes that are exposed at low tide in optically complex fjords in Greenland remains unclear. In particular, the FAI was designed to distinguish floating algae from open water and implicit in the definition is the assumption that reflectance in the red, NIR, and SWIR results from algae (or other floating vegetation). In contrast to an open ocean setting, other sources of red, NIR and SWIR reflectance may be found in optically complex fjord systems, especially those with icebergs and when the intertidal zone is included. Optically complex environments like iceberg-impacted fjords in Greenland, therefore, may contain vegetated pixels with different sources of background reflectances. In this case, exposed, intertidal macrophytes must be distinguished from sand, rock, and/or mud, open water, which may be clear, highly turbid, or somewhere in between, and icebergs, bergy bits, and brash ice. Large iceberg sails are easily detected but smaller icebergs, shallow, underwater ice rams, and adjacency effects (mixed ice and water pixels) can be difficult to distinguish from other sources of reflectance and, therefore, misclassified. The ability of the vegetation indices and SMA to identify intertidal macrophytes in optically complex fjords in Greenland will depend on the spectral characteristics of these different sources of background reflectance.

This paper tests three hypotheses: I) 10-m S2-MSI imagery and commonly used detection methods can identify intertidal macrophytes that are exposed at low tide in an optically complex fjord system in Greenland impacted by marine and land terminating glaciers; II) floating macrophytes accumulate in patches that are sufficiently large to be detected by 10-m S2-MSI images; III) iceberg scour and turbid meltwater runoff shape the spatial distribution of intertidal macrophytes. These hypotheses are especially timely given the rapid retreat of marine-terminating glaciers in Greenland (Carr et al., 2017; Wood et al., 2018) and the potential contribution of macrophytes in Greenland to Blue Carbon stocks. Iceberg calving will cease when marine terminating glaciers retreat onto land, eliminating iceberg scour, which may increase the habitat available for intertidal macrophytes in Greenland. The results of this paper can also inform future *in situ* studies to ensure optimal usage of limited field resources.

2. Materials and methods

2.1. Study area

The boundaries of the study area extend from 63.90°N, 51.999°W in the southwest to 64.01°N, 51.302°W in the northeast encompassing the marine areas of Nuup Kangerlua (NK; also referred to as Godthåbsfjord), Kobbefjord, and Ameralik in southwest Greenland (Fig. 1). NK is approximately 190 km long, with a coastal perimeter of 984 km and a surface area of 2188 km². Situated to the south of NK is Ameralik, which is approximately 75 km long (Stuart-Lee et al., 2021) with a marine area of 388 km² and a coastal perimeter of 283 km. The mouths of the fjords join at the southwest, near Greenland's capital city of Nuuk, where they connect to the continental shelf (Fig. 1B). Their combined marine area is 2770 km² with a coastline of 1300 km.

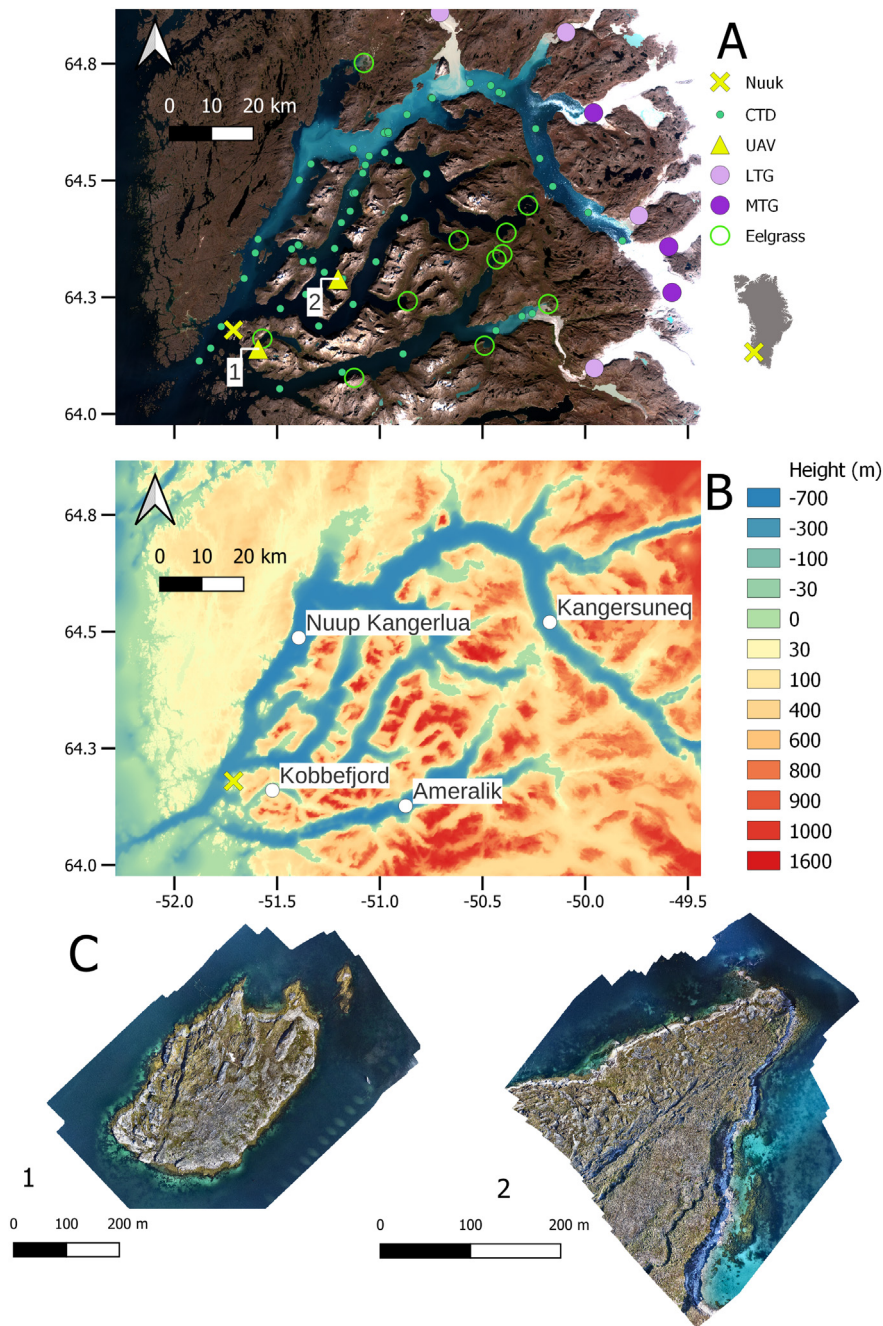


Fig. 1. (A) The capital city of Nuuk is indicated by the yellow cross in the main map and the inset map of Greenland. Locations of eelgrass meadows were retrieved from Olesen et al. (2015) and are indicated by open green circles. The small green dots represent the locations of *in situ* CTD observations. Two UAS validation site locations are marked with yellow triangles and numbers. Marine and land-terminating glaciers are indicated by dark and light purple circles, respectively. (B) The study area includes Nuup Kangerlua, Kobbefjord, and Ameralik. The topography of the study area from BedMachine v5. (C) The two UAS orthomosaics used to validate the S2-MSI results. The numbers correspond to the locations in panel (A). (For interpretation of the references to colour in this figure legend, the reader is referred to the web version of this article.)

The coastal boundaries of the NK and Ameralik systems consist largely of bedrock (Gustavson et al., 2020) with some sand/gravel beaches and mud banks (Fenger-Nielsen et al., 2020). With the exception of the low-lying terrain that forms the northwest boundary of NK, the coastal margins consist primarily of steeply-sloped mountains, though shallow and gently sloping bathymetry can be found in some small bays (Fig. 1B). The maximum depths of the fjord systems exceeds 700 m (Fig. 1B). The fjords experience maximum tidal ranges of 4–5 m during spring tides (Richter et al., 2011).

Three marine-terminating glaciers and three land-terminating glaciers are found within the boundaries of NK (Fig. 1A; Mortensen et al., 2011).

Kangersuneq, the inner part of NK, is characterized by high iceberg concentrations and the middle and outer parts of NK are impacted by a turbid plume that originates from the glacier-fed Tasersuaq (Arendt et al., 2011). Sea ice covers the inner part of NK during the winter. Ameralik is impacted by turbid meltwater runoff from a land terminating glacier near the head of the fjord (Hudson et al., 2014; Stuart-Lee et al., 2021). Ameralik, therefore, is free of icebergs and sea ice cover is limited to the river delta in winter (Stuart-Lee et al., 2021).

In western Greenland, dominant intertidal macroalgae communities include *Ascophyllum nodosum*, and *Fucus* spp, which are exposed at low tide (Ørberg et al., 2018; Thyrring et al., 2021). Subtidal kelps are dominated

by species such as *Saccharina latissima* and *Agarum clathratum* in deeper waters (Krause-Jensen et al., 2012). Dense eelgrass meadows of *Z. marina* also occur in NK, Kobbefjord, and Ameralik and their locations, as reported in Olesen et al. (2015), are shown in Fig. 1. The macrophytes found in the study area do not produce canopies that float on the sea surface.

2.2. S2-MSI images

To avoid sea ice, S2-MSI Level-1C (L1C) images that were acquired between the months of May and September from 2016 to 2021 were downloaded from the Copernicus Sentinel Hub. The study area was contained in S2-MSI tiles T22WDS and T22WES. In total, 76 cloud-free scenes (as determined by visual inspection of the browse images) of the study area were downloaded.

The workflow to estimate the spatial extents of icebergs, turbidity, intertidal macrophytes is summarized in Fig. A.1. ACOLITE merged the two tiles covering NK and Ameralik and the top-of-atmosphere (TOA) reflectance in the 20 m and 60 m bands was resampled to 10 m.

A land mask was constructed using a S2-MSI image that was acquired on 30 July 2017 at high tide (Carlson, 2022). Land was masked by applying a threshold of 0.1 Wm^{-2} to the top-of-atmosphere reflectance in the 1614 nm SWIR band. Mountain lakes and shaded coastal regions were masked using the DEM. The coastal margin was visually inspected for outliers and edited when necessary. The land mask was applied to restrict the assessments of cloud cover and terrain shadows to the marine domain.

Cloud masks were computed for each image by applying a threshold of 0.0015 Wm^{-2} to TOA reflectance at 1375 nm. ACOLITE was then used to compute Rayleigh-corrected reflectances (R_{RC}) in the 26 images (see Table A.1) with $>2\%$ cloud cover over the marine area. Pixels with $R_{RC} < 0$ were masked, though this accounted for $<0.003\%$ of the marine area. These images were used to estimate the spatial extents of icebergs and turbidity (see section 2.2.1).

To identify exposed, intertidal macrophytes the 26 S2-MSI images with $<2\%$ cloud cover were further filtered according to tide and terrain shadows. Images obtained when the tide height exceeded $\sim 1 \text{ m}$ and where terrain shadows impacted $>2\%$ of the coastal area were excluded. Four S2-MSI images remained after applying the tide and terrain shadow criteria. Two images that were acquired at or near high tide were included to quantify the effects of water level on intertidal macrophyte detection.

2.2.1. Icebergs and turbidity

High iceberg concentrations and high turbidity were identified in the 26 cloud-free images to test the hypothesis that iceberg scour and/or high turbidity shape the spatial distribution of macrophytes. Icebergs were detected by applying a threshold to TOA reflectance in the green band (559 nm or 560 nm for S2A and S2B, respectively). The threshold varied from 0.21 Wm^{-2} to 0.24 Wm^{-2} and was adjusted in each image to find the optimal value that detected the most ice while avoiding the turbid river plumes. The threshold was used to create a binary iceberg mask where ice and non-ice pixels were assigned values of 1 and 0, respectively. The ice mélange extent was computed from the iceberg mask by quantifying the number ice pixels in a $500 \text{ m} \times 500 \text{ m}$ macropixel. High ice concentration was defined as macropixels containing $>25\%$ ice (>625 pixels). The mélange extent was defined as the contour that enclosed $500 \text{ m} \times 500 \text{ m}$ macropixels whose average exceeded 0.25.

Turbidity was computed using the Dogliotti product embedded in ACOLITE (Dogliotti et al., 2015). Bare areas in optically shallow water and small bits of ice that were not detected by the iceberg threshold appeared as pixels with very high (e.g., $>1900 \text{ FTU}$) turbidity. These very high values were masked in the turbidity maps. Disentangling the reflectance from turbid waters and small, sub-pixel-sized, pieces of ice can be challenging (Hodgkins et al., 2016) and one can easily be mistaken for the other. Erroneous turbidity values caused by small bits of ice that were not detected by the brightness threshold were removed by dilating the iceberg mask by 5 pixels. Small bits of ice that remained appeared as individual pixels or small groups of pixels, similar to specular image noise. A 2D

median filter with a 5×5 pixel window was applied to smooth out this noise. A threshold of 10 FNU was used to identify pixels with high turbidity and a turbidity binary image was then constructed where high turbidity pixels were assigned a value of 1 and low turbidity pixels were assigned a value of 0. The same $500 \text{ m} \times 500 \text{ m}$ macropixel grid was applied to the binary image and contours were extracted that enclosed regions where the mean exceeded 0.25. The 67 *in situ* turbidity measurements (see section 2.3.1) that were collected within one day of a cloud-free S2-MSI image were used to validate satellite-derived turbidity, resulting in 21 matchups.

2.2.2. Spectral endmembers

Average endmember spectra for five classes were extracted from S2-MSI images using SNAP. The five classes included icebergs ($n = 1023$), bare (un-vegetated) bottom ($n = 1023$), clear water ($n = 1023$), turbid water ($n = 1023$), and exposed intertidal macroalgae ($n = 256$; Fig. 2). Endmember spectra selection areas differed from the validation sites that were surveyed by the UAS. Icebergs, turbid water, and clear water were visually identified in the S2-MSI images. The exposed, intertidal macroalgae endmember spectrum was obtained from a coastal area north of Nuuk (Fig. A.2), which is known to the authors. Similarly, the bare endmember spectrum was obtained from the mouth of the fjord, which is an area that is also known to the authors (Fig. A.3).

2.2.3. Vegetation indices

Macrophytes were detected by applying thresholds to the NDVI, EVI, and FAI. The optimal thresholds were identified by comparing the S2 classification accuracy to the UAS imagery. The locations of eelgrass beds were obtained from Olesen et al. (2015) and no effort was made to distinguish macroalgae from eelgrass as they appear spectrally similar in the multispectral S2-MSI imagery (Wilson et al., 2020).

Based on an assessment of the NDVI, EVI, FAI, and SMA in two optically complex environments, only the NDVI was used to identify macrophytes in the entire study area (see section 3.1). The NDVI threshold that produced the highest accuracy in the UAS validation sites differed between sites one (0.25) and two (0.4) and the more conservative value (0.4) was used to identify macrophytes in the entire study area.

The NDVI threshold was used to construct binary images whereby macrophyte and non-macrophyte pixels were assigned values of 1 and 0, respectively. Connected pixels were then identified in the binary images. Single pixels that were not connected to others were removed, as observations of macrophytes in the study area suggest that they occur in long coastal bands, for coastal, intertidal macrophytes, or in elongated streaks, for floating mats, that would span multiple 10 m S2-MSI pixels (Ager et al., n.d.,

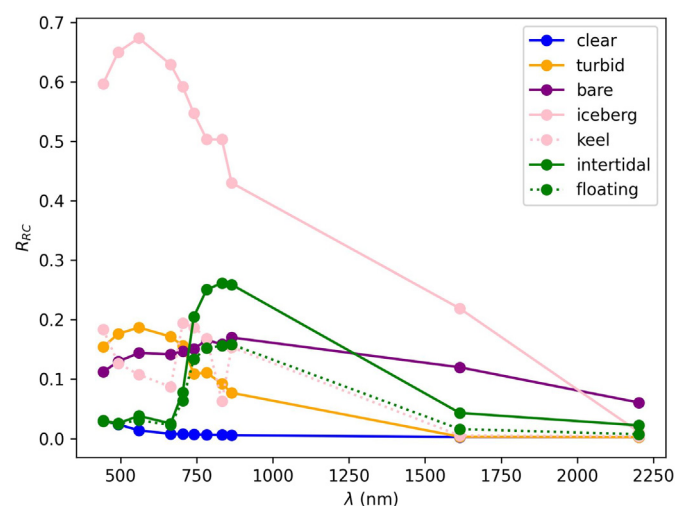


Fig. 2. Average endmember spectra for clear, turbid, bare, iceberg, and intertidal macrophytes are plotted with solid lines. The dashed lines indicate reflectance from iceberg keels and floating macroalgae, which are spectrally similar.

Submitted). Macrophytes were separated into intertidal and floating categories based on the distance of a macrophyte pixel to the nearest land pixel. Macrophyte pixels that were 100 m or more from the nearest land pixel were classified as floating.

2.3. Supporting data

This study relies on publicly available data and measurements that were previously acquired either by the authors or through public sources. All raster data, including S2-MSI and UAS orthomosaics, were projected to UTM Zone 22 N (WGS 84).

2.3.1. In situ profiles of turbidity and photosynthetically active radiation

In situ measurements of turbidity and photosynthetically active radiation (PAR) that were obtained in the months of May to September from 2016 to 2020 were aggregated into a single database. Sixty-seven profiles were obtained using a Seabird SBE-19-plus CTD that was equipped with a Li-Cor Spherical PAR sensor and SeaPoint turbidity sensor. The majority of these profiles (62) were collected during measurement campaigns that were conducted from the Greenland Institute of Natural Resources. Five profiles were obtained from the Greenland Ecosystem Monitoring (GEM) program. The profile locations are shown in Fig. 1A. The vertical diffuse attenuation coefficient of PAR (K_{dPAR}) was estimated from the slope of the natural logarithm of PAR *versus* depth. The *in situ* profiles of turbidity and K_{dPAR} are used to validate S2-derived turbidity and to visualize spatial patterns of light availability, respectively.

2.3.2. UAS aerial imagery

Aerial images from two locations in NK were surveyed in July 2017 (Fig. 1A,C) using a DJI Phantom 3 UAS during the Mission Arctic citizen science expedition (Carlson et al., 2021). UAS imagery from a third site was also available through the Greenland Ecosystem Monitoring Program - Nuuk Basis monitoring of marine flora (<http://g-e-m.dk/>) but suitable S2-MSI images could not be found due to clouds and tides.

The Phantom 3 captured 12 megapixel still digital images using a gimbal-stabilized camera. The Phantom 3 missions (sites one and two) were flown manually in an approximate grid pattern to ensure sufficient overlap between images for processing with Structure from Motion (SfM) photogrammetry software. Images were processed using Agisoft Metashape Professional (v7.1) following the United States Geological Service (USGS) protocols for coastal imagery (Over et al., 2021). Section B in the appendix provides UAS image processing details.

The UAS-derived orthomosaics were used to cross-validate the macrophytes that were detected in the S2 images by finding the closest matchup date with favorable cloud and tide conditions. The UAS-derived DEM was used to create a land mask for the orthomosaic. Both UAS orthomosaics were resampled to 0.1 m resolution to provide a common resolution. Macroalgae were identified in UAS orthomosaics by applying thresholds to the RGB images in QGIS. The S2-MSI pixels were used to construct a 10 m grid in each UAS orthomosaic. Grid cells were classified as land, water, or macrophytes. 10 m grid cells that contained >75 % macrophyte pixels were classified as macrophytes. The no-data mask for each UAS orthomosaic was applied to the corresponding S2-MSI NDVI image. The S2-MSI NDVI was also classified as either land, water, or macrophytes (Fig. 3). The UAS validation was used to find threshold values for the S2-derived vegetation indices that resulted in the highest producer, user, and overall accuracy for each class. Note that UAS validation sites lacked turbid water and icebergs.

2.3.3. Tide and terrain data

Modeled tide data for Nuuk were obtained from the Danish Meteorological Institute (http://ocean.dmi.dk/tides/tides_grl.uk.php). The 90 m TanDEM-X digital elevation model produced by the German Aerospace Center (Wessel et al., 2018) was used in the hillshade function in Matlab (Hebeler, 2022) to compute a terrain shadow mask for each S2-MSI image.

3. Results and discussion

3.1. Hypothesis I: SMA and NDVI, EVI, and FAI can identify exposed, intertidal macrophytes in optically complex fjords in Greenland

Figs. 4 and 5 demonstrate the performance of the vegetation indices and the SMA in areas with high iceberg concentrations and exposed mudbanks, respectively. The examples in Figs. 4 and 5 are derived from the S2-MSI image acquired on 10 July 2017 and they are representative of all these sources of optical complexity in all images that were analyzed. In Fig. 4A, the RGB composite image shows large icebergs and many smaller bits of ice. The EVI and FAI mis-classified icebergs as macrophytes (Fig. 4B-C). The NDVI did not detect macrophytes in the inner fjord (Fig. 4D). The SMA shows elevated macrophyte abundances (>0.3) around the margins of icebergs (Fig. 4E). The SMA iceberg abundance identified the sails of large icebergs (Fig. 4F) but comparison with the RGB composite (Fig. 4A) shows that it failed to identify smaller bits of ice. Comparing the turbidity abundance (Fig. 4G) to the RGB composite (Fig. 4A) shows that the smaller bits of ice were mis-classified as turbidity. Note the absence of macrophytes on the coastal margins (Fig. 4B-G).

Assuming that the SMA, EVI, and FAI results in Fig. 4 were accurate and that the inner fjord contains abundant floating macrophytes, the next logical question is where did they come from if intertidal macrophytes were not detected along the coastal margins? Floating macrophytes drift passively in response to prevailing currents so surface Lagrangian transport could have carried them into the inner fjord. However, during summer, estuarine circulation dominates in NK (Mortensen et al., 2011) and the net surface transport flows away from the glaciers toward the mouth of the fjord. Macrophytes floating in the inner fjord could not have been transported from downstream sources and, therefore, would have had local origins. Furthermore, while some floating macroalgae may be found floating around icebergs, the probability that they are found around the margin of every iceberg is very low. Instead, mis-classification of icebergs as macrophytes by the SMA, EVI, and FAI is the more likely explanation.

Exposed mudbanks were visible at low tide in the RGB image of the Tasersuaq outflow in Fig. 5A. The FAI and EVI misclassified mudbanks as macrophytes (Fig. 5B-C). The NDVI (Fig. 5A), on the other hand, did not classify exposed mudbanks as vegetation. The SMA shows elevated macrophyte abundances on the mudbanks (Fig. 5D). The iceberg endmember correctly identified the grounded icebergs that are visible in the bottom of the image (Fig. 5E). The turbidity endmember correctly identified the turbid plume but could not distinguish between turbid water and mudbanks (Fig. 5F).

The apparent failure of the SMA, EVI, and FAI in areas with high iceberg concentrations and exposed mudbanks can be explained by examining the reflectance spectra (Fig. 2). With regards to the SMA, similarities between the endmembers result in misclassifications. In particular, the spectra of iceberg margins and iceberg keels were also very similar to floating macroalgae (dashed lines in Fig. 2). Threshold adjustments to the FAI, EVI, and SMA did not remove false positives in either the iceberg-congested inner fjord or areas with bare substrate.

The misclassification of icebergs as macrophytes is likely due to the reflectance from iceberg keels (Fig. 4H). In summer, relatively warm (>0°C) surface waters lead to the production of subsurface ice 'rams' or protrusions that extend away from the iceberg just below the surface (Wagner et al., 2014). Methods to address the effects of iceberg keel reflectance on macrophyte detection schemes have yet to be reported. Icebergs and bare bottom (including mudbanks, sand, and bedrock) exhibited high reflectance in the red, NIR, and SWIR wavelengths (Fig. 2) that resulted in elevated values in the FAI and EVI that were misinterpreted as macrophytes.

The iceberg keel and floating macroalgae spectra exhibit a difference in the NIR reflectance (Fig. 2) that could be exploited when classifying macrophytes in pro-glacial fjord systems with high concentrations of ice. The mean iceberg keel reflectance spectrum exhibits a dip at 833 nm, whereas the mean floating macroalgae spectrum increases (Fig. 2). Thus, iceberg keels may be excluded by masking pixels using the difference $R_{833} - R_{865}$, though this may be too restrictive in areas that are not impacted by ice.

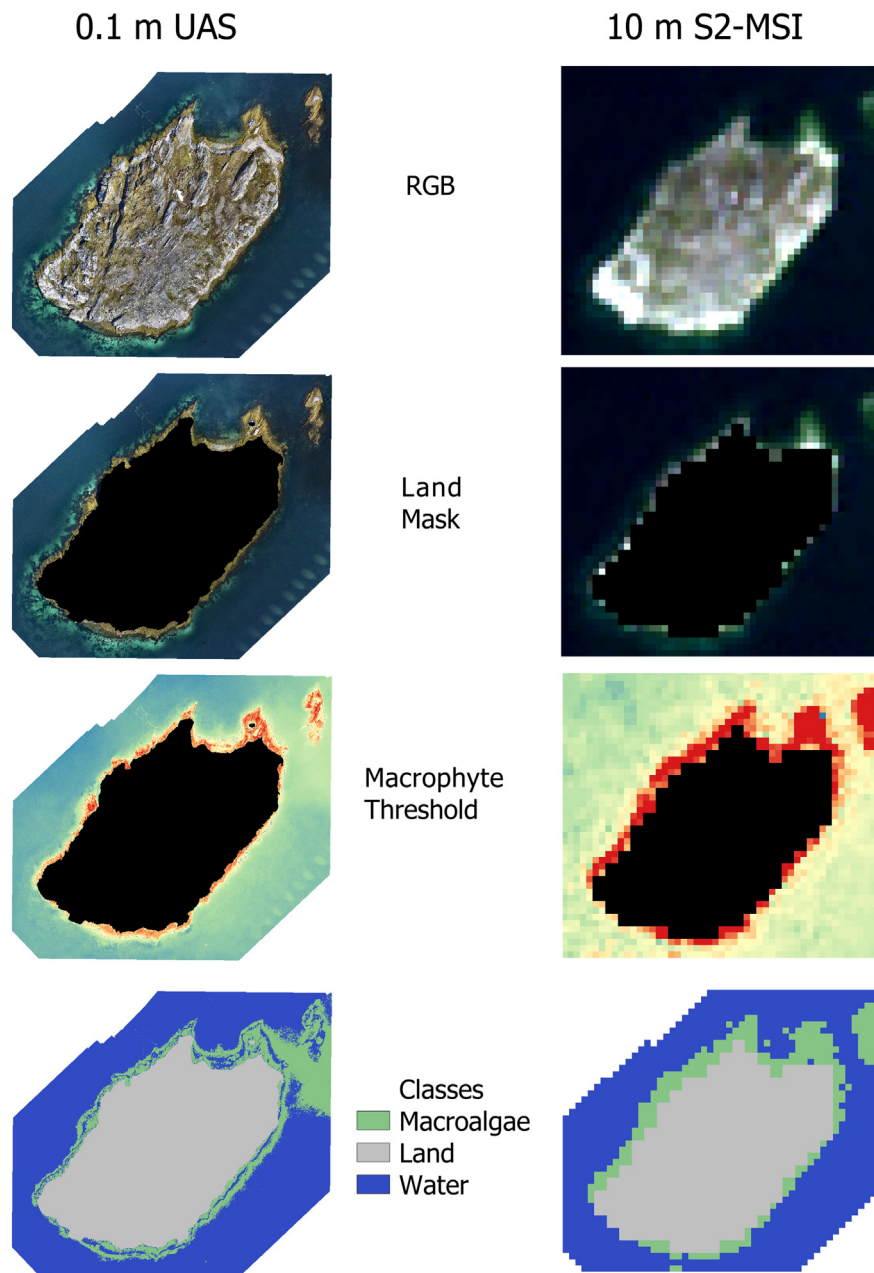


Fig. 3. The validation of the classification of 10 m S2-MSI NDVI images using 0.1 m UAS orthomosaics is illustrated here using site 1 and the same process was applied at site 2 (see Fig. 1A for locations). Land was masked (black pixels), intertidal macrophytes were detected using a threshold, and a classified image was produced.

The simplistic assumption could be made that sources of high reflectance, including icebergs, bare bottom, and very turbid waters, indicate areas that do not support macrophyte growth. Under this assumption, the brightness threshold was lowered to mask any pixels with TOA reflectance in the green band that exceeded 0.15 Wm^{-2} . This approach, however, did not mask small bits of brash ice that were characterized by lower reflectances, perhaps because of their size or because they were wet. These small bits of brash ice were then misclassified as macrophytes by the SMA, FAI, and EVI. Alternatively, one could assume that hypothesis III is correct and that iceberg scour prevents macrophytes from growing in the intertidal zone in the inner fjord. Under this assumption the entire inner fjord could be neglected. This approach, however, would not allow any future expansion of macrophytes into the inner fjord to be detected, nor would it solve the problem of masking small icebergs that reach the middle and outer fjord or the misclassification of exposed bare bottom elsewhere in the fjords.

With regard to hypothesis I, the NDVI appears to be insensitive to the optical complexity introduced by icebergs and exposed, bare, exposed intertidal substrates. As a result, the NDVI was used to quantify the distributions of intertidal and floating macrophytes in the study area. Intertidal macrophytes identified in S2-MSI-derived NDVI images were compared to 0.1 m resolution UAS orthomosaics of two validation sites in NK (Figs. 1 and 3). The overall accuracy was 90 % at site one and 89 % at site two. The user accuracy varied from 49 % at site one to 76 % at site two. The producer accuracy varied from 50 % at site one to 67 % at site two. The higher number of false positives and omissions at site one may be explained by the difference of 0.3 m in tide height between the UAS and S2-MSI images. Note that the UAS validation imagery lacked turbid plumes and icebergs, which should be remedied in future studies. The user and producer's accuracies and kappa values for all three classes (macrophytes, land, and water) is presented in Table B.2.

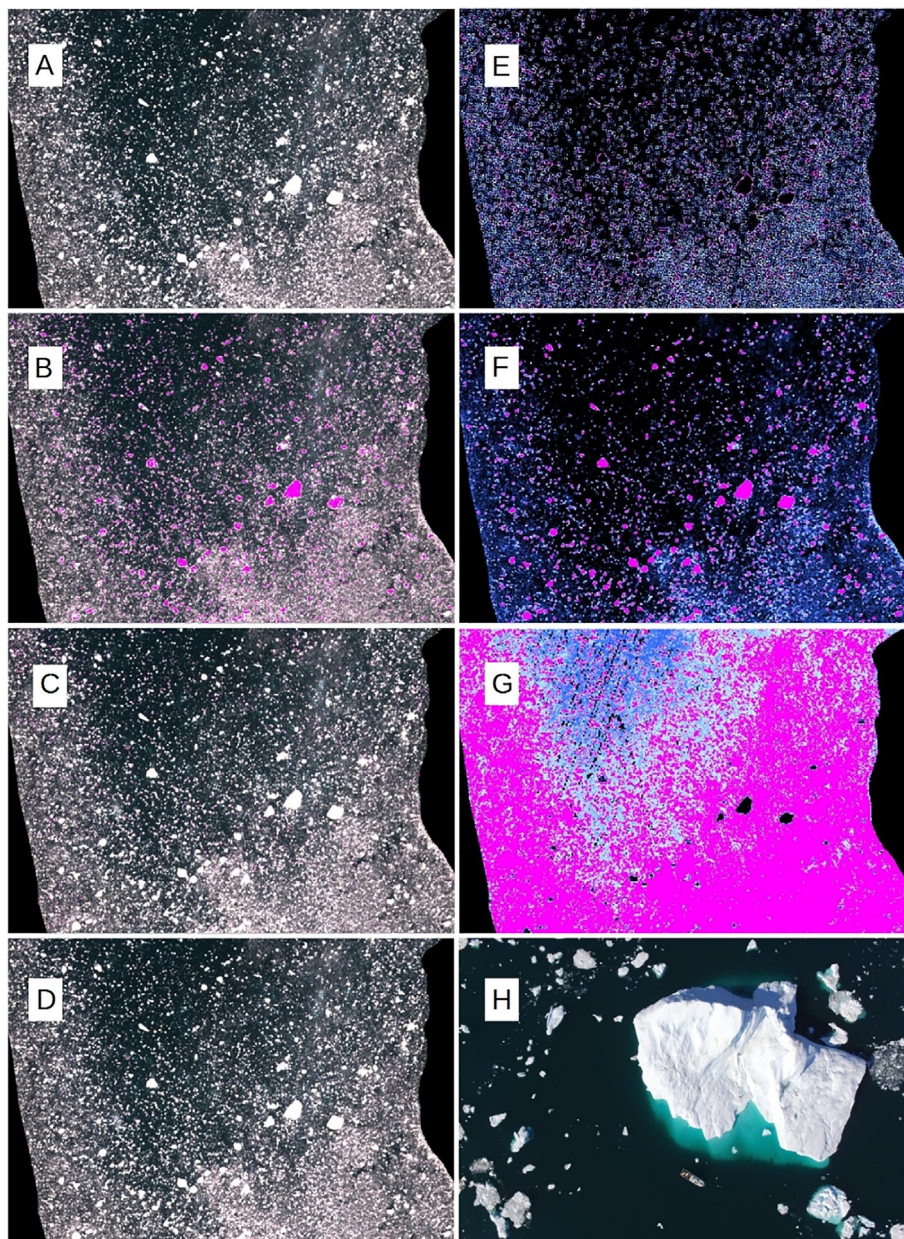


Fig. 4. (A) A S2-MSI RGB composite image from the inner part of NK on 10 July 2017. Panels B–D show the RGB image with the macrophyte masks for the EVI, FAI, and NDVI overlaid in bright pink. Panels E–G show the SMA intertidal macrophyte abundance, iceberg abundance, and turbidity abundance, respectively, with abundances >0.3 masked with bright pink. In panels A–G black areas represent the land mask. (H) A UAS image in the inner part of NK shows a large iceberg with a shallow keel protrusion. (For interpretation of the references to colour in this figure legend, the reader is referred to the web version of this article.)

NDVI thresholds of 0.4 and 0.25 produced the highest accuracy at sites one and two, respectively. The more conservative NDVI threshold of 0.4 was used to identify intertidal macrophytes that were exposed at low tide in the entire study area (Fig. 6). The NDVI threshold of 0.4 is higher than bare sand values of 0–0.12 reported by Wilson et al. (2020) and higher than terrestrial bare soil values of 0.2 reported by Montandon and Small (2008).

Intertidal macrophyte coverage at low-tide varied from 10 km² to 16 km² (Fig. 6A–D). At high tide, intertidal macrophyte coverage dropped to 0.34 km² to 1.36 km² (Fig. 6E–F). The total intertidal macrophyte cover was estimated by finding intertidal macrophyte pixels that were present in at least three of the four low-tide macrophyte images. This approach resulted in an intertidal macrophyte cover of 12.04 km² and their locations are shown in Fig. 7. The 12 km² coverage of intertidal macrophytes is likely conservative because shallow sub-tidal macrophytes were excluded and terrain shadows obscured some areas. The NDVI appears to have identified

known eelgrass meadows (Olesen et al., 2015) but no attempt was made to distinguish eelgrass from macroalgae (see section 2.2.3). High NDVI values in known eelgrass meadow locations could also result from the accumulation of detached, drifting macroalgae (Barillé et al., 2010).

3.2. Hypothesis II: Floating macrophytes accumulate in patches that are sufficiently large to be detected by 10-m S2-MSI images

The locations of floating mats of macrophytes are shown in light green in Fig. 6. The total area covered by floating macrophytes ranged from 0.07 km² to 1.36 km² (Fig. 6). Floating macrophytes were most common around the skerry islands at the mouth of the fjord and at the intersections of fjords. Fig. A.4 shows an example of large floating mat near the mouth of Ameralik in the image acquired on 10 July 2017. Individual mats of floating macrophytes ranged in area from 400 m² to 326,800 m². Thus, floating macrophytes accumulate in patches that are sufficiently large to be detected in

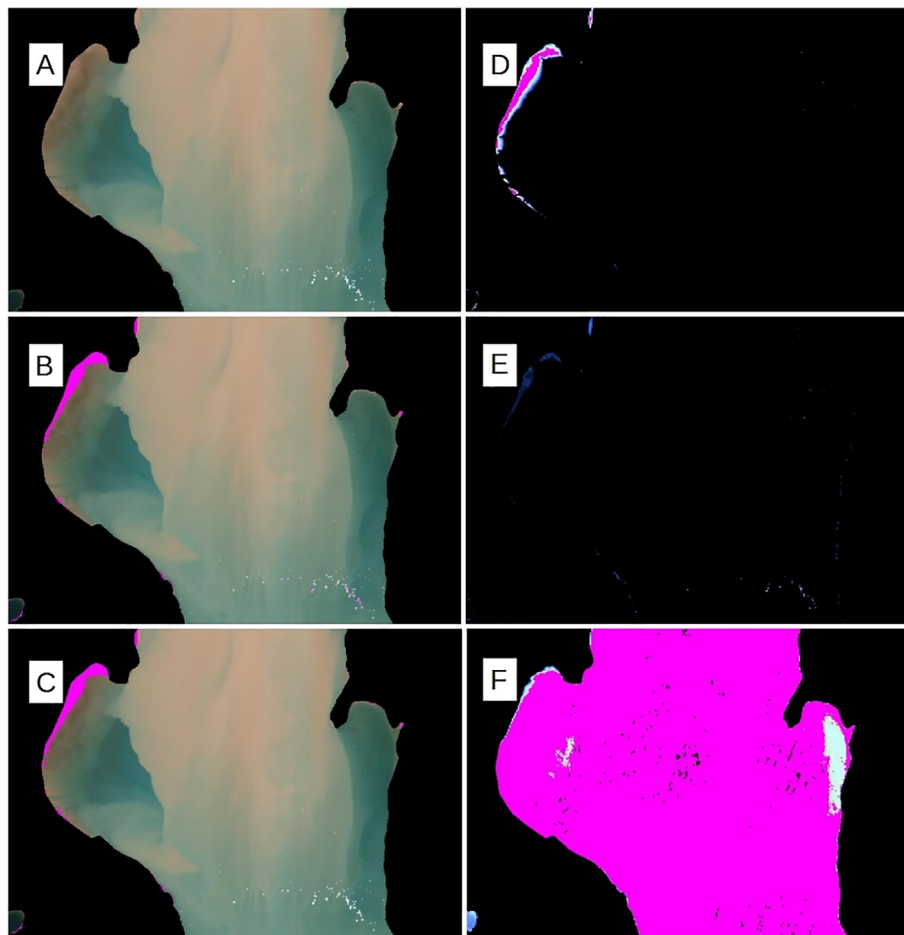


Fig. 5. (A) A S2-MSI RGB composite image from the Tasersuaq outflow from the image acquired on 10 July 2017. The NDVI macrophyte vegetation mask is overlaid on the RGB image in panel (A). Note the absence of macrophytes detected by the NDVI. Panels B-C show the RGB image with the macrophyte masks for the EVI and FAI overlaid in bright pink. Panels D-F show the SMA intertidal macrophyte abundance, iceberg abundance, and turbidity abundance, respectively, with abundances >0.3 masked with bright pink. (For interpretation of the references to colour in this figure legend, the reader is referred to the web version of this article.)

10-m S2-MSI images using the NDVI. A field study in NK found floating macroalgae throughout the fjord with an average biomass of 55 kg wet weight km^{-2} and observations confirm the accumulation of floating biomass near the mouth of the fjord (Ager et al. 2022).

3.3. Hypothesis III: Iceberg scour and turbid meltwater runoff shape the spatial distribution of intertidal macrophytes

The locations of intertidal macrophytes that were present in at least three of the four low-tide macrophyte images are shown in Fig. 7. The contour lines of high iceberg concentrations and turbid plumes are also shown. The intertidal macrophyte distribution exhibits very little spatial overlap with the high iceberg and turbidity contours. Intertidal macrophytes were not found in Kangarsuneq, from the Tasersuaq plume to the head of the fjord (Fig. 7). High iceberg concentrations were consistently found in the inner fjord, consistent with Mortensen et al. (2014) who found that the subsurface heat transport causes the majority of the glacial ice to melt in the inner fjord. Elevated turbidity was consistently observed from Kangarsuneq to the middle of the fjord at Qoornup Ikinngua, where NK branches into three arms (Fig. 7). High turbidity also occurred at Qugssuk (Fig. 7), where dense eelgrass meadows have been reported (Olesen et al., 2015). Glacial meltwater runoff impacted the inner part of Ameralik (Hudson et al., 2014). The CTD-derived K_{dPAR} values also show the highest light attenuation in the inner parts of NK and Ameralik (Fig. 7). These results suggest that turbidity-induced light limitations and/or iceberg scour may play

a role in shaping the spatial distribution of intertidal macrophytes in the study area.

The iceberg scour hypothesis assumes that intertidal macrophytes can recover from the episodic disturbance caused by the grounding of a single iceberg. On the other hand, repeated scouring by iceberg collisions with the fjord margins prevents macrophytes from settling in regions with a persistent presence of high concentrations of icebergs and frequent scouring. Thus, fjord regions that are characterized by high iceberg concentrations and frequent scouring should not support intertidal macrophytes. Conversely, macrophytes should be found in areas where the risk of repeated iceberg scouring is low, due to an absence of icebergs and/or the presence of a physical protective barrier. The spatial distribution of glacial ice in NK is controlled by melt-driven subsurface heat transport, which is currently about an order of magnitude larger than the calving flux from the glacier (Mortensen et al., 2014). Climate change could affect the area of impacted iceberg scour. In the near-term, changes in fjord circulation and heat exchange processes could alter the submarine melt rate of icebergs in the inner fjord. On longer time scales, the retreat of marine terminating glaciers onto land and the cessation of iceberg calving could open up the inner fjord to colonization by macrophytes, most likely macroalgae.

The turbidity hypothesis is based on the light requirements for photosynthetic organisms and the previously-established relationship between suspended particulate matter and light attenuation. Areas impacted by persistent high turbidity should be light-limited and, therefore, should not support macrophytes. While the iceberg size distribution has not been

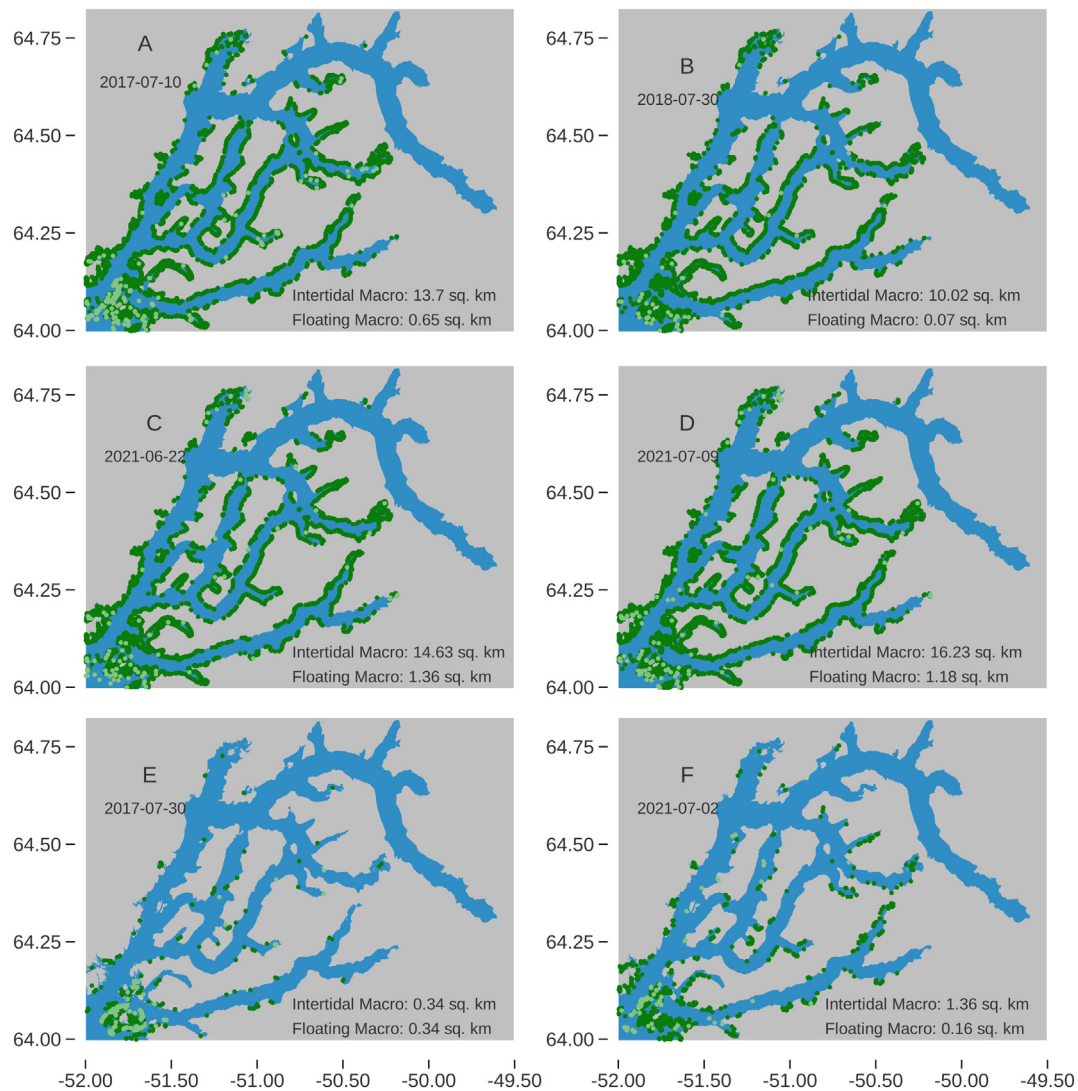


Fig. 6. The distribution of intertidal (dark green) and floating (light green) macrophytes in the study area for the four low-tide S2-MSI images (A-D) and the two high-tide images (E-F). The respective areas of intertidal and floating macrophyte cover are indicated in each panel. (For interpretation of the references to colour in this figure legend, the reader is referred to the web version of this article.)

reported for NK, most of the glacial ice in the fjord consists of small icebergs and bergy bits (Carlson et al., 2017). Bergy bits and brash ice have length scales that are the same order of magnitude as the 10 m S2-MSI pixels, which makes them more difficult to detect and increases the chances of mis-classifying them as turbid water (Hodgkins et al., 2016). Even when the sails of larger icebergs can be detected in the 10 m S2-MSI imagery, their margins introduce optical complexity that impacts the detection of macrophytes. Iceberg-induced optical complexity may arise through adjacency effects or reflectance from submerged ice ‘rams’ (Fig. 4H).

While turbid freshwater runoff intermittently enters the fjord at Qugssuk through a small stream, this area is also characterized by shallow waters and some of the high turbidity could, in fact, be due to bottom reflectance. Dense beds of eelgrass (*Zostera marina*) are found at Qugssuk and just north of the river delta at the head of Ameralik (Olesen et al., 2015), despite the presence of turbid water.

Turbidity may not limit light in the shallow intertidal zone to the extent that macrophytes cannot grow. Instead, multiple stressors likely act to limit the distribution of intertidal macrophytes. In the river plumes, low salinity combined with high turbidity and sedimentation rates may prevent macrophytes from growing. Similarly, in the inner part of NK, macrophyte growth may be limited by the combination of iceberg scouring and high turbidity.

Limited anecdotal observations suggest that macroalgae can be found in the iceberg-congested inner part of NK. These macroalgal beds may be obscured by the high iceberg concentrations and/or steep coastal margins and terrain shadows.

A robust turbidity algorithm for glacier-impacted waters has yet to be developed. The Dogliotti algorithm was used here given relatively good agreement with *in situ* turbidity. The 21 matchups between *in situ* CTD measurements of S2-derived turbidity computed from the Dogliotti algorithm are shown in Fig. A.5A. The least-squares linear fit to all data points indicates that the Dogliotti algorithm overestimates high turbidity values (e.g., >10 FTU). High turbidity values are under-represented in the *in situ* data, however, and when only values from 0 to 10 FTU are considered the Dogliotti algorithm underestimates the lower values (Fig. A.5B). Despite the disagreements between the absolute values, the fits account for most of the variance in the data (Fig. A.5), which suggests that the Dogliotti algorithm is at least sufficient for quantifying spatial gradients in turbidity. Other turbidity algorithms include the Nechad (Nechad et al., 2010), ANTA (Klein et al., 2021) and exponential fits to reflectance in the red and NIR (Hudson et al., 2014; Schild et al., 2017). The available *in situ* data are not sufficient to evaluate these algorithms. Future studies should develop turbidity algorithms that resolve the

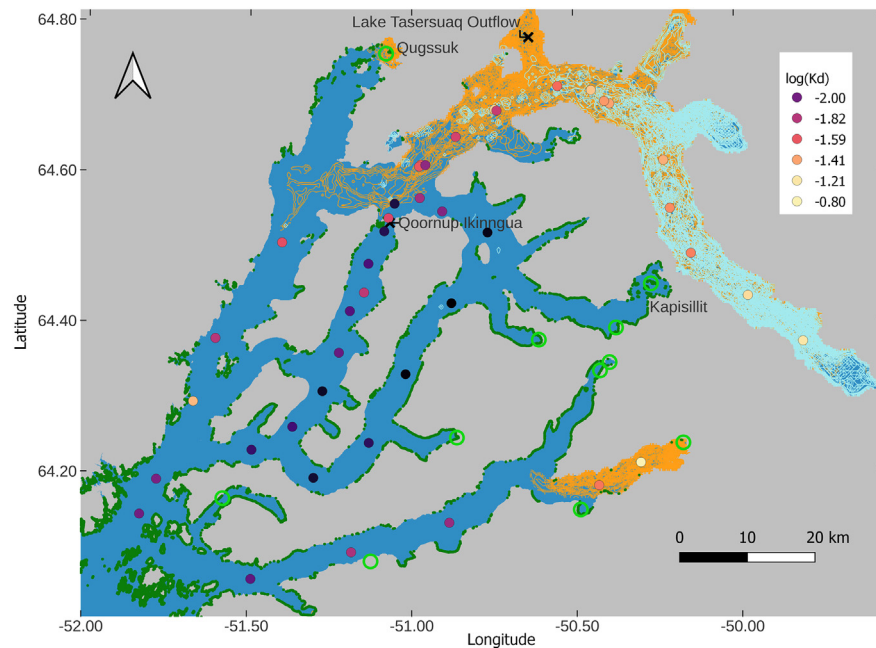


Fig. 7. Small, dark green points indicate locations where intertidal macrophytes were detected in at least three of the four low-tide S2-MSI images. Light blue lines and orange lines indicate contours of high iceberg and high turbidity concentrations, respectively, from the 26 cloud-free S2-MSI images. Colored dots indicate the logarithm of the CTD-derived vertical diffuse attenuation coefficient of PAR (K_{dPAR}). Eelgrass meadows are indicated by open green circles (positions were obtained from Olesen et al., 2015). (For interpretation of the references to colour in this figure legend, the reader is referred to the web version of this article.)

wide range of values found in glacially impacted fjords that often contain both very clear and highly turbid waters.

The brightness threshold applied to TOA reflectance at 560 nm to detect iceberg sails varied from 0.21 Wm^{-2} to 0.24 Wm^{-2} , which lies within the range of values used in panchromatic Landsat images (Scheick et al., 2019; Sulak et al., 2017). Other methods to identify icebergs have also been tested and may be useful in future studies. Heiselberg and Heiselberg (2017) distinguished between icebergs and ships in S2-MSI images of NK using a supervised classification method that identified pixels that deviated from the background reflectance. Moyer et al. (2019) and Rezvanbehbahani et al., 2020 applied a brightness threshold to the 10 m S2-MSI near-infrared band (band 8; 833 nm) to identify icebergs in fjords in east Greenland.

4. Conclusions

This paper tested three hypotheses: I) 10-m S2-MSI imagery and commonly used detection methods can identify intertidal macrophytes that are exposed at low tide in an optically complex fjord system in Greenland impacted by marine and land terminating glaciers; II) floating macrophytes accumulate in patches that are sufficiently large to be detected by 10-m S2-MSI images; III) iceberg scour and turbid meltwater runoff shape the spatial distribution of intertidal macrophytes. With regard to hypothesis I, the NDVI is best suited for studies of intertidal macrophytes in optically complex, glacially impacted fjord systems with large tidal ranges. The other indices tested, namely the EVI and the FAI, resulted in false positives around icebergs and exposed, bare substrate, which reflected in the red, NIR, and SWIR. SMA also produced false positives in these environments due to spectral similarities in the endmembers. In particular, iceberg keel reflectance posed a unique, and unexpected problem as it was spectrally similar to floating macroalgae. Approximately 12 km^2 of exposed, intertidal macrophytes were found in low-tide S2-MSI images.

With regard to hypothesis II, floating mats of macrophytes were detected in S2-MSI imagery. Floating macrophytes were most common

around the skerry islands at the mouth of the fjord and at the intersections of fjords. The total area covered by floating macrophytes ranged from 0.07 km^2 to 1.36 km^2 and individual mats of floating macrophytes ranged in area from 400 m^2 to $326,800 \text{ m}^2$. The detection of floating mats of macrophytes in S2-MSI NDVI images could assist in estimates of the contributions of coastal macrophyte communities to offshore, deep-water carbon sinks.

With regard to hypothesis III, exposed, intertidal macrophyte locations did not overlap with regions of high iceberg concentration or elevated turbidity, suggesting that iceberg scouring and turbidity play a role in shaping the spatial distributions of macrophytes in fjords with marine terminating glaciers. Thus, the spatial distribution of exposed, intertidal macrophytes as well as the drivers of their spatial distribution (icebergs and turbidity) were determined from a single remote sensing dataset. The methods presented here can be applied to quantify climate-change-induced shifts in intertidal macrophytes distributions in fjord systems that contain retreating marine terminating glaciers.

The sources of optical complexity apply to most fjords in Greenland and, therefore, the methodology may be extended to produce a Greenland-wide estimate of shallow marine vegetation. Future studies should focus on subtidal macrophyte communities by collecting high-resolution bathymetry and *in situ* radiometry. Additional UAS surveys should be conducted to extend the availability of very-high-resolution validation imagery into regions with turbid plumes and icebergs.

Funding

This research was supported by the Independent Research Fund Denmark (8021-00222 B, 'CARMA').

CRedit authorship contribution statement

Daniel F. Carlson: Conceptualization, Methodology, Software, Validation, Formal analysis, Investigation, Resources, Data curation, Writing – original draft, Writing – review & editing, Visualization. **Antoni Vivó-Pons:** Methodology, Software, Validation, Formal analysis, Investigation,

Writing – review & editing. **Urs A. Treier**: Methodology, Software, Resources, Writing – review & editing. **Eva Mätzler**: Methodology, Software, Resources, Data curation, Writing – review & editing. **Lorenz Meire**: Data curation, Writing – review & editing. **Mikael Sejr**: Conceptualization, Data curation, Writing – original draft, Writing – review & editing. **Dorte Krause-Jensen**: Conceptualization, Writing – original draft, Writing – review & editing, Project administration, Funding acquisition.

Data availability

Sources of publicly available data are stated in the manuscript. Datasets produced by the authors are available on Zenodo (links provided in the manuscript)

Appendix A. Sentinel-2 imagery

The workflow used to process and analyze Sentinel-2 (S2) images of the study area is summarized in Fig. A.1. The date, tide height, and cloud coverage of the 26 S2 images analyzed for icebergs and turbidity are summarized in Table A.1. The six S2 images analyzed for macrophytes are indicated in bold in Table A.1.

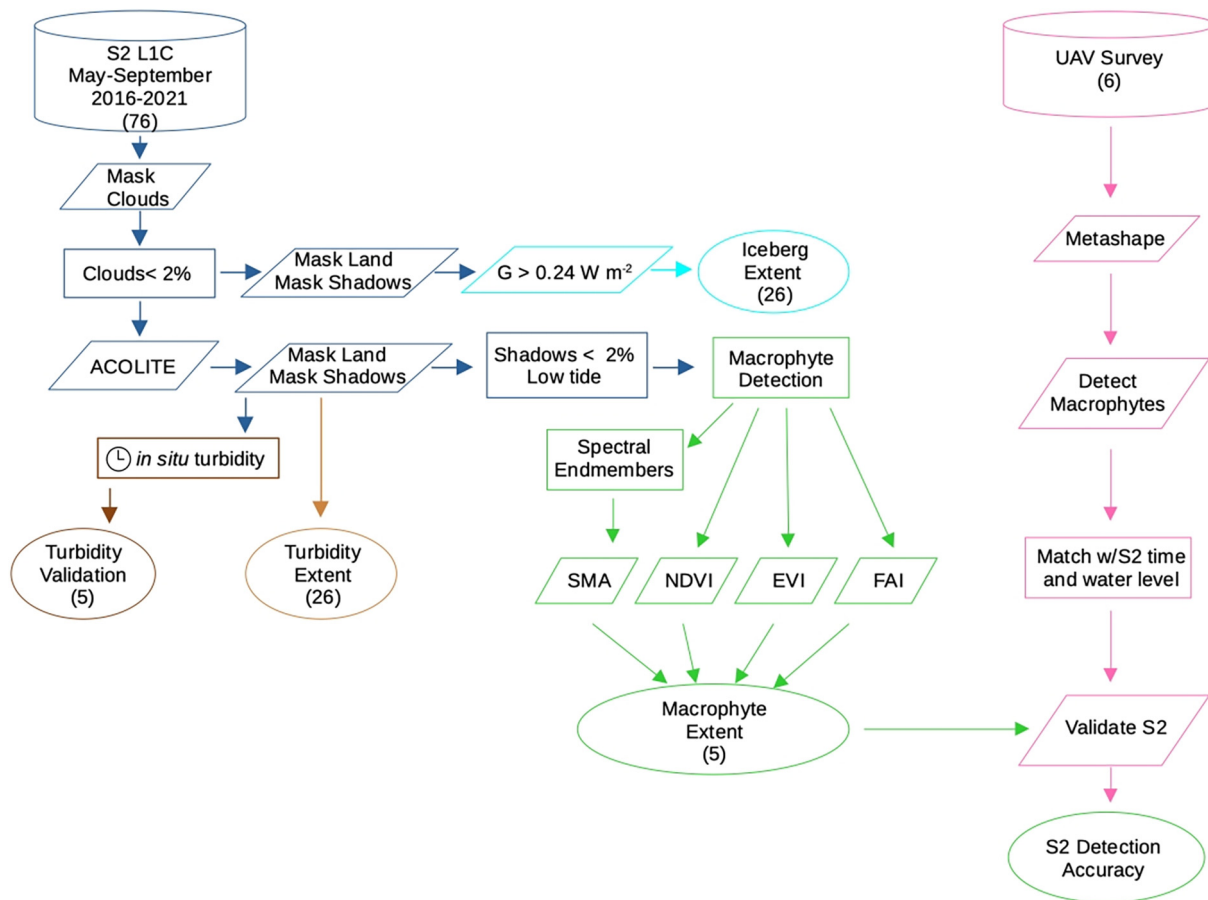


Fig. A.1. The workflow used to select and process S2-MSI images is summarized here.

Table A.1

The dates, tide height, and cloud coverage of the 26 Sentinel-2 images used to compute iceberg concentrations and turbid plume extents are summarized. Cloud coverage is presented as total area and the percentage of the marine area impacted by clouds. The six images that were analyzed for intertidal macrophytes are indicated in bold.

Date	Tide (m)	Cloud coverage (km ² /%)
2016-07-25	3.4	0.24/8.5e-3
2016-07-28	2.9	7.8/0.28
2016-08-14	2.2	1.7/6.1e-2
2016-09-23	3.9	53.5/1.93
2016-09-26	2.3	130/4.7
2017-05-31	3.3	0.59/2.1e-2
2017-07-10	1.0	32.1/1.2

Table A.1 (continued)

Date	Tide (m)	Cloud coverage (km ² /%)
2017-07-30	3.5	46.4/1.7
2018-05-09	2.6	625/22.6
2018-07-13	0.9	470/17.0
2018-07-30	1.2	0.03/1e-3
2018-09-18	2.8	286/10.3
2019-08-29	0.6	197/7.1
2020-05-20	1.1	61.9/2.23
2021-05-13	1.7	10.8/0.4
2021-06-22	1.3	5.3/0.19
2021-07-02	2.9	0.29/1e-2
2021-07-09	1.1	4.8/0.17
2021-08-31	3.0	998/36
2021-09-05	1.0	236/8.5
2021-09-10	2.5	51.9/1.9
2021-09-15	3.0	96/0.96
2021-09-17	2.0	26.7/0.96
2021-09-25	2.8	648/23.4

Intertidal macroalgae that were exposed at low tide are visible around the capital city of Nuuk, Greenland (see Fig. 1A for location) in Bing aerial imagery (Fig. A.2A) and appear as high (0.4–0.9) NDVI in Sentinel-2 imagery (Fig. A.2B). Intertidal macroalgae that were exposed at low tide around Nuuk were used to compute the average intertidal macrophyte spectral endmember for the spectral mixture analysis (SMA; see section 2.2.2). Similarly, bare sand can be found in areas in near the mouth of the fjord and these areas are visible in Bing aerial imagery (Fig. A.3A) and correspond to lower (0.05–0.15) NDVI values (Fig. A.3B). These bare sand areas were used to compute the average bare spectral endmember for SMA (see section 2.2.2).

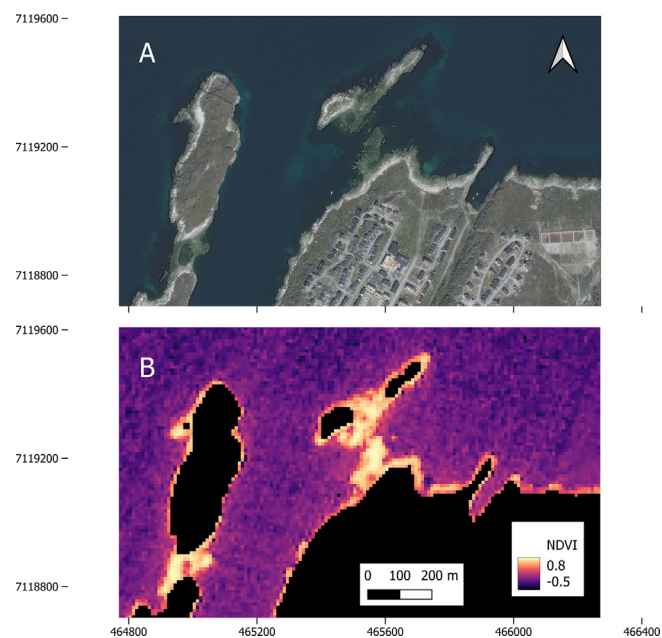


Fig. A.2. (A) Dense macroalgal beds are visible in a Bing aerial image of the town of Nuuk, Greenland. (B) The same area is shown in a Sentinel-2 derived NDVI image at low tide on 10 July 2017. The black pixels correspond to land and high NDVI is indicated by yellow-white pixels. Coordinates on the x and y axes correspond to positions, in units of meters, in UTM Zone 22 N (WGS 84).

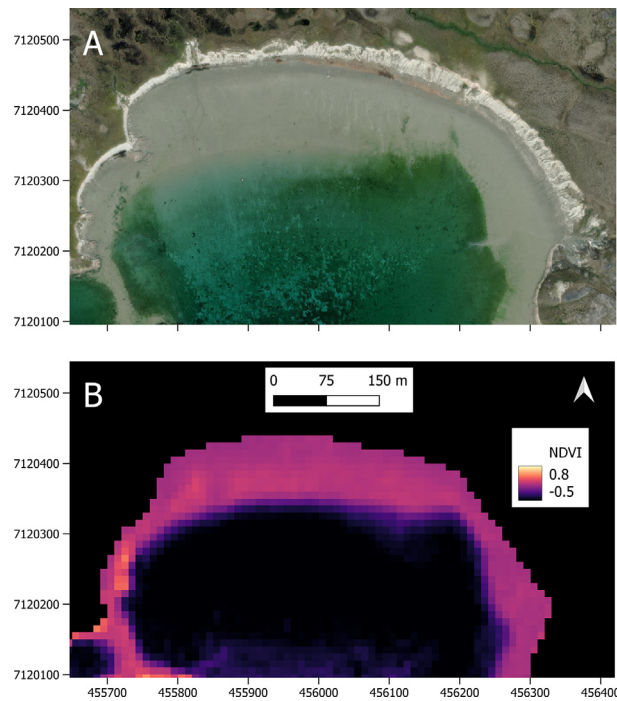


Fig. A.3. (A) Bare sand is visible in a Bing aerial image of the coast near the mouth of the fjord. (B) The same area is shown in a Sentinel-2 derived NDVI image at low tide on 10 July 2017. Coordinates on the x and y axes correspond to positions, in units of meters, in UTM Zone 22 N (WGS 84).

An example of a large floating mat of what is most likely macroalgae is shown in Fig. A.4. The floating mat is visible in both the RGB composite image (Fig. A.4A) and the NDVI (Fig. A.4B). This image was extracted from the S2 image that was acquired on 10 July 2017.

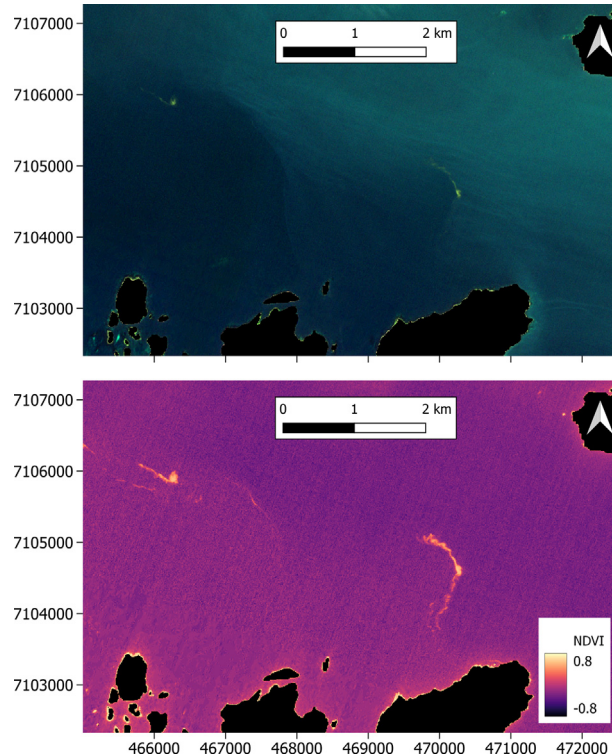


Fig. A.4. Large floating mats of macrophytes are visible near the mouth of Ameralik fjord in (A) an RGB composite image and (B) in the NDVI from 10 July 2017. Coordinates on the x and y axes correspond to positions, in units of meters, in UTM Zone 22 N (WGS 84).

The matchups between the *in situ* CTD-derived surface turbidity and the turbidity estimated from the Dogliotti (Dogliotti et al., 2015) algorithm included with ACOLITE are shown in Fig. A5. The entire dataset is shown in Fig. A.5A and turbidity values that exceed 10 FTU are excluded in Fig. A.5B.

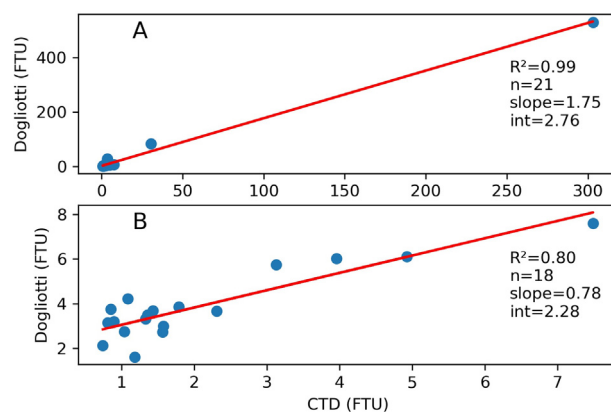


Fig. A.5. Matchups between *in situ* surface turbidity measurements and corresponding S2-derived turbidity values are displayed as scatter plots over (A) the full range of values observed and (B) over values of 0–10 FTU. The red lines denote the least squares linear fit to the data. The coefficient of determination, number of values, slope, and intercept are also provided. Note that the fit is not forced through the origin. (For interpretation of the references to colour in this figure legend, the reader is referred to the web version of this article.)

Appendix B. UAS image acquisition and processing

The UAS surveys of sites one and two (see Fig. 1A for locations) are summarized in Table B.1. The confusion matrix for the three classes (macrophytes, land, and water) for the comparison between UAS and S2 NDVI are shown in Table B.2.

Table B.1

The date, number of images, altitude, ground sampling distance (GSD), reprojection error, ground control point (GCP) error, total area covered, equivalent number of 10 m Sentinel-2 pixels, and the digital object identifier for each UAS dataset are summarized here.

Site	Date	No. Img.	Tide (m)	Alt. (m)	GSD (m)	Reproj. Err. (pix)	GCP Err. (m)	Area (km ²)	No. S2 Pix.	DOI
1	2017-07-05	128	1.3	153	0.05	0.32	0.59	0.261	1956	https://doi.org/10.5281/zenodo.7066580
2	2017-07-11	225	0.8	76	0.025	0.31	0.42	0.102	1006	https://doi.org/10.5281/zenodo.7066573

During manual missions, the Phantom 3 flew at a constant altitude and acquired still images at five second intervals. The UAS hovered when images were acquired and changed position during the five second interval between images. To account for the large contrast in brightness between marine and terrestrial areas the exposure value was set to -1 . Lowering the exposure value prevented overexposure of images that contained both bright terrestrial and darker marine areas. This manual flight approach resulted in high-quality images, in terms of focus and contrast.

Images were aligned in Agisoft Metashape using the ‘high’ accuracy setting, key point and tie point limits of 60,000 and 0, respectively, and generic and reference preselection (Over et al., 2021). After alignment, GCPs were added to improve the overall accuracy of the georectification. GCPs were added by identifying prominent rocks in either Google Earth or Bing Satellite imagery, similar to methods employed by Azim et al. (2019) and Rossiter et al. (2019).

After adding GCPs, the intrinsic and extrinsic camera parameters were optimized. Next, low-quality tie points were removed using an iterative gradual selection process based on three accuracy measures. These accuracy measures included the reconstruction uncertainty, projection accuracy, and reprojection error (see Over et al., 2021 for details). Initial thresholds were specified for each accuracy measure, as well as a maximum percentage of tie points to remove during each iteration. If the number of points selected for removal did not exceed the maximum threshold then the threshold was adjusted until the maximum was reached. The camera parameters were optimized after each set of low-accuracy tie points was removed.

The remaining high-accuracy tie points were then used to compute the dense point cloud. The dense point cloud was computed using the ‘ultra-high’ accuracy, ‘mild’ depth filtering, ‘calculate point colors’, and ‘calculate point confidence’ options. Outliers in the dense cloud were removed by selecting points with confidences between 0 and 2. Any remaining ‘fliers’ and/or ‘sinks’ were manually removed. The dense cloud was then used to compute a digital elevation model (DEM). An orthomosaic was computed after the DEM. Orthomosaics and DEMs were exported as geotiffs that were reprojected to UTM Zone 22 N (WGS 84).

Table B.2

The user and producer accuracies for UAS validation sites one and two (see Fig. 1 for locations) are summarized. The values in parentheses indicate the NDVI thresholds that resulted in the highest accuracies. The kappa value for each class is also indicated.

Site	NDVI (0.4)	User Accuracy	Producer Accuracy	Kappa
1	Macroalgae	48.62	50.62	0.41
	Land	94.56	94.44	0.91
	Water	90.12	89.26	0.81
NDVI (0.25)				
2	Macroalgae	76.48	67.24	0.72
	Land	94.91	99.62	0.89
	Water	85.81	84.42	0.79

References

- Ager, T.G., Krause-Jensen, D., Sejr, M.K., Olesen, B., Carlson, D.F., Winding, M.H.S., .. High biomass of floating macroalgae supports carbon sequestration potential within and beyond a Greenland fjord. Submitted to Science of the Total Environment <http://ssrn.com/abstract=4246828>.
- Arendt, K.E., Dutz, J., Jonasdottir, S.H., Jung-Madsen, S., Mortensen, J., Moller, E.F., Nielsen, T.G., 2011. Effects of suspended sediments on copepods feeding in a glacial influenced sub-Arctic fjord. *J. Plankton Res.* 33, 1526–1537. <https://doi.org/10.1093/plankt/fbr054>.
- Azim, S., Rasmussen, J., Nielsen, J., Gislum, R., Laursen, M.S., Christensen, S., 2019. Manual geo-rectification to improve the spatial accuracy of ortho-mosaics based on images from consumer-grade unmanned aerial vehicles (UAVs). *Precis. Agric.* 20, 1199–1210. <https://doi.org/10.1007/s11119-019-09647-9>.
- Barillé, L., Robin, M., Harin, N., Bargain, A., Launeau, P., 2010. Increase in seagrass distribution at Bourgneuf Bay (France) detected by spatial remote sensing. *Aquat. Bot.* 92, 185–194. <https://doi.org/10.1016/j.aquabot.2009.11.006>.
- Bayley, D., Brickle, P., Brewin, P., Golding, N., Pelembe, T., 2021. Valuation of kelp forest ecosystem services in the Falkland Islands: a case study integrating blue carbon sequestration potential. *One Ecosyst.* 6, e62811. <https://doi.org/10.3897/oneeco.6.e62811>.
- Bell, T.W., Cavanaugh, K.C., Siegel, D.A., 2015. Remote monitoring of giant kelp biomass and physiological condition: an evaluation of the potential for the hyperspectral infrared imager (HyspIRI) mission. *Remote Sens. Environ.* 167, 218–228. <https://doi.org/10.1016/j.rse.2015.05.003>.
- Bell, T.W., Allen, J.G., Cavanaugh, K.C., Siegel, D.A., 2020. Three decades of variability in California's giant kelp forests from the Landsat satellites. *Remote Sens. Environ.* 238, 110811. <https://doi.org/10.1016/j.rse.2018.06.039>.
- Carlson, D.F., 2022. A 10 m Land Mask for the Nuup Kangerlua, Kobbefjord, and Ameralik Fjord Systems in Southwest Greenland. <https://doi.org/10.5281/zenodo.7376540> Dataset uploaded to Zenodo. Last accessed 29 November 2022.
- Carlson, D.F., Boone, W., Meire, L., Abermann, J., Rysgaard, S., 2017. Bergy bit and melt water trajectories in Godthåbsfjord (SW Greenland) observed by the expendable ice tracker. *Front. Mar. Sci.* 4, 276. <https://doi.org/10.3389/fmars.2017.00276>.
- Carlson, D.F., Carr, G., Crosbie, J.L., Lundgren, P., Peissel, N., Pett, P., Turner, W., Rysgaard, S., 2021. The 2017 Mission Arctic citizen science sailing expedition conductivity, temperature, and depth profiles in Western Greenland and Baffin Bay. *Front. Mar. Sci.* 8, 665582. <https://doi.org/10.3389/fmars.2021.665582>.
- Carpenter, S., Byfield, V., Felgate, S.L., Price, D.M., Andrade, V., et al., 2022. Using unoccupied aerial vehicles (UAVs) to map seagrass cover from Sentinel-2 imagery. *Remote Sens.* 14, 477. <https://doi.org/10.3390/rs14030477>.
- Carr, J.R., Stokes, C.R., Vieli, A., 2017. Threefold increase in marine-terminating outlet glacier retreat rates across the Atlantic Arctic: 1992–2010. *Ann. Glaciol.* 58, 72–91. <https://doi.org/10.1017/aog.2017.3>.
- Cavanaugh, K.C., Siegel, D.A., Reed, D.C., Dennison, P.E., 2011. Environmental controls of giant-kelp biomass in the Santa Barbara Channel, California. *Mar. Ecol. Prog. Ser.* 429, 1–17. <https://doi.org/10.3354/meps09141>.
- Cavanaugh, K.C., Bell, T., Costa, M., Eddy, N.E., Gendell, L., et al., 2021. A review of the opportunities and challenges for using remote sensing for management of surface-canopy forming kelps. *Front. Mar. Sci.* 8, 753531. <https://doi.org/10.3389/fmars.2021.753531>.
- Cottier, F.R., Nilsen, F., Skogseth, R., Tverberg, V., Skardhamar, J., et al., 2010. Arctic fjords: a review of the oceanographic environment and dominant physical processes. *Geol. Soc. Lond., Spec. Publ.* 344, 35–50. <https://doi.org/10.1144/SP344.4>.
- Dogliotti, A.I., Ruddick, K.G., Nechad, B., Doxaran, D., Knaeps, E., 2015. A single algorithm to retrieve turbidity from remotely-sensed data in all coastal and estuarine waters. *Remote Sens. Environ.* 156, 157–168. <https://doi.org/10.1016/j.rse.2014.09.020>.
- Drusch, M., Del Bello, U., Carlier, S., Colin, O., Fernandez, V., 2012. Sentinel-2: ESA's optical high-resolution mission for GMES operational services. *Remote Sens. Environ.* 120, 25–36. <https://doi.org/10.1016/j.rse.2011.11.026>.
- Duffy, J.E., Benedetti-Cecchi, L., Trinanes, J., Muller-Karger, F.E., Ambo-Rappe, R., et al., 2019. Toward a coordinated global observing system for seagrasses and marine macroalgae. *Front. Mar. Sci.* 6, 317. <https://doi.org/10.3389/fmars.2019.00317>.
- Fenger-Nielsen, R., Elberling, B., Kroon, A., Westergaard-Nielsen, A., Matthiesen, H., et al., 2020. Arctic archaeological sites threatened by climate change: a regional multi-threat assessment of sites in south-west Greenland. *Archaeometry* 62, 1280–1297. <https://doi.org/10.1111/arcm.12593>.
- Filbee-Dexter, K., Wernberg, T., Fredriksen, S., Norderhaug, K.M., Pedersen, M.F., 2019. Arctic kelp forests: diversity, resilience and future. *Glob. Planet. Chang.* 172, 1–14. <https://doi.org/10.1016/j.gloplacha.2018.09.005>.
- Finger, D.J.I., McPherson, M.L., Houskeeper, H.F., Kudela, R.M., 2021. Mapping bull kelp canopy in northern California using Landsat to enable long-term monitoring. *Remote Sens. Environ.* 254, 112243. <https://doi.org/10.1016/j.rse.2020.112243>.
- Friedlander, A.M., Ballesteros, E., Bell, T.W., Giddens, J., Henning, B., et al., 2018. Marine biodiversity at the end of the world: Cape Horn and Diego Ramírez islands. *PLOS ONE* 13, e0189930. <https://doi.org/10.1371/journal.pone.0189930>.
- Gustavson, K., Hansson, S.V., van Beest, F.M., Fritt-Rasmussen, J., Lassen, P., et al., 2020. Natural removal of crude and heavy fuel oil on rocky shorelines in Arctic climate regimes. *Water Air Soil Pollut.* 231, 479. <https://doi.org/10.1007/s11270-020-04850-1>.
- Hamilton, S.L., Bell, T.W., Watson, J.R., Grorud-Colvert, K.A., Menge, B.A., 2020. Remote sensing: generation of long-term kelp bed data sets for evaluation of impacts of climatic variation. *Ecology* 101, e03031. <https://doi.org/10.1002/ecy.3031>.
- Hebeler, P., 2022. Hillshade: function to calculate hillshade for a digital elevation model. <http://www.mathworks.com/matlabcentral/fileexchange/14863-hillshade> Last accessed 29 March 2022.
- Heiselberg, P., Heiselberg, H., 2017. Ship-iceberg discrimination in Sentinel-2 multispectral imagery by supervised classification. *Remote Sens.* 9, 1156. <https://doi.org/10.3390/rs9111156>.
- Hodgkins, R., Bryant, R., Darlington, E., Brandon, M., 2016. Pre-melt-season sediment plume variability at Jökulsárlón, Iceland, a preliminary evaluation using in-situ spectroradiometry and satellite imagery. *Ann. Glaciol.* 57, 39–46. <https://doi.org/10.1017/aog.2016.20>.
- Høgslund, S., Sejr, M.K., Wiktor, J., Blicher, M.E., Wegeberg, S., 2014. Intertidal community composition along rocky shores in south-west Greenland: a quantitative approach. *Polar Biol.* 37, 1549–1561. <https://doi.org/10.1007/s00300-014-1541-7>.
- Hopwood, M.J., Carroll, D., Dunse, T., Hodson, A., Holding, J.M., et al., 2020. Review article: how does glacier discharge affect marine biogeochemistry and primary production in the Arctic? *Cryosphere* 14, 1347–1383. <https://doi.org/10.5194/tc-14-1347-2020>.
- Hu, C., 2009. A novel ocean color index to detect floating algae in the global oceans. *Remote Sens. Environ.* 113, 2118–2129. <https://doi.org/10.1016/j.rse.2009.05.012>.
- Hudson, B., Overeem, I., McGrath, D., Syvitski, J.P.M., Mikkelsen, A., Hasholt, B., 2014. MODIS observed increase in duration and spatial extent of sediment plumes in Greenland fjords. *Cryosphere* 8, 1161–1176. <https://doi.org/10.5194/tc-8-1161-2014>.
- Huete, A.R., Justice, C., 1999. *MODIS Vegetation Index (MOD13) Algorithm Theoretical Basis Document Ver. 3*. 1999.
- Huovinen, P., Ramírez, J., Palacios, M., Gómez, I., 2020. Satellite-derived mapping of kelp distribution and water optics in the glacier impacted Yendegai Fjord (Beagle Channel, Southern Chilean Patagonia). *Sci. Total Environ.* 703, 135531. <https://doi.org/10.1016/j.scitotenv.2019.135531>.
- Jensen, J.R., 1980. Remote sensing techniques for kelp surveys. *Photogramm. Eng.* 46, 743–755.
- Johannessen, S.C., 2022. How can blue carbon burial in seagrass meadows increase long-term, net sequestration of carbon? A critical review. *Environ. Res. Lett.* 17, 093004. <https://doi.org/10.1088/1748-9326/ac8ab4>.
- Johnston, D.W., 2019. Unoccupied aircraft systems in marine science and conservation. *Annu. Rev. Mar. Sci.* 11, 439–463. <https://doi.org/10.1146/annurev-marine-010318-095323>.
- Joyce, K.E., Duce, S., Leahy, S.M., Leon, J., Maier, S.W., 2019. Principles and practice of acquiring drone-based image data in marine environments. *Mar. Freshw. Res.* 70, 952. <https://doi.org/10.1071/MF17380>.
- Keshava, N., 2003. A survey of spectral unmixing algorithms. *Lincoln Lab J.* 14, 55–78.
- Klein, K.P., Lantuit, H., Heim, B., Doxaran, D., Juhs, B., et al., 2021. The Arctic Near-shore Turbidity Algorithm (ANTA) - a multi sensor turbidity algorithm for Arctic nearshore environments. *Sci. Remote Sens.* 4, 100036. <https://doi.org/10.1016/j.srs.2021.100036>.
- Kotta, J., Valdivia, N., Kutser, T., Töming, K., Rätsep, M., Orav-Kotta, H., 2018. Predicting the cover and richness of intertidal macroalgae in remote areas: a case study in the Antarctic Peninsula. *Ecol. Evol.* 8, 9086–9094. <https://doi.org/10.1002/ece3.4463>.
- Krause-Jensen, D., Marbà, N., Olesen, B., Sejr, M.K., Christensen, P.B., et al., 2012. Seasonal sea ice cover as principal driver of spatial and temporal variation in depth extension and annual production of kelp in Greenland. *Glob. Chang. Biol.* 18, 2981–2994. <https://doi.org/10.1111/j.1365-2486.2012.02765.x>.
- Krause-Jensen, D., Duarte, C.M., 2014. Expansion of vegetated coastal ecosystems in the future Arctic. *Front. Mar. Sci.* 1, 77. <https://doi.org/10.3389/fmars.2014.00077>.
- Krause-Jensen, D., Duarte, C.M., 2016. Substantial role of macroalgae in marine carbon sequestration. *Nat. Geosci.* 9, 737–742. <https://doi.org/10.1038/ngeo2790>.
- Krause-Jensen, D., Sejr, M.K., Bruhn, A., Rasmussen, M.B., Christensen, P.B., et al., 2019. Deep penetration of kelps offshore along the west coast of Greenland. *Front. Mar. Sci.* 6, 375. <https://doi.org/10.3389/fmars.2019.00375>.
- Krause-Jensen, D., Archambault, P., Assis, J., Bartsch, I., Bischof, K., et al., 2020. Imprint of climate change on pan-Arctic marine vegetation. *Front. Mar. Sci.* 7, 617324. <https://doi.org/10.3389/fmars.2020.617324>.
- Kuhwald, K., Schneider von Deimling, J., Schubert, P., Oppelt, N., 2021. How can Sentinel-2 contribute to seagrass mapping in shallow, turbid Baltic Sea waters? *Remote Sens. Ecol. Conserv.* 8, 328–346. <https://doi.org/10.1002/rse2.246>.
- Kutser, T., Hedley, J., Giardino, C., Roelfsema, C., Brando, V.E., 2020. Remote sensing of shallow waters – a 50 year retrospective and future directions. *Remote Sens. Environ.* 240, 111619. <https://doi.org/10.1016/j.rse.2019.111619>.
- Lebrasse, M.C., Schaeffer, B.A., Coffey, M.M., Whitman, P.J., Zimmerman, R.C., et al., 2022. Temporal stability of seagrass extent, leaf area, and carbon storage in St. Joseph Bay, Florida: a semi-automated remote sensing analysis. *Estuar. Coasts*, 45. <https://doi.org/10.1007/s12237-022-01050-4>.
- Légaré, B., Bélanger, S., Singh, R.K., Bernatchez, P., Cusson, M., 2022. Remote sensing of coastal vegetation phenology in a cold temperate intertidal system: implications for classification of coastal habitats. *Remote Sens.* 14, 3000. <https://doi.org/10.3390/rs14133000>.
- Loring, D.H., Asmund, G., 1996. Geochemical factors controlling accumulation of major and trace elements in Greenland coastal and fjord sediments. *Environ. Geol.* 28, 2–11. <https://doi.org/10.1007/s002540050072>.
- Lôugas, L., Kutser, T., Kotta, J., Vahtmäe, E., 2020. Detecting long time changes in benthic macroalgal cover using Landsat image archive. *Remote Sens.* 12, 1901. <https://doi.org/10.3390/rs12111901>.
- Main-Knom, M., Pflug, B., Louis, J., Debaecker, V., Müller-Wilm, U., et al., 2017. *Sen2Cor for Sentinel-2*. In *Image and Signal Processing for Remote Sensing XXIII*. vol. 10427, pp. 37–48. SPIE doi:Sen2Cor for Sentinel-2.
- Marbà, N., Krause-Jensen, D., Olesen, B., Christensen, P.B., Merzouk, A., et al., 2017. Climate change stimulates the growth of the intertidal macroalgae *Ascophyllum nodosum* near the northern distribution limit. *Ambio* 46, 119–131. <https://doi.org/10.1007/s13280-016-0873-7>.
- Marbà, N., Krause-Jensen, D., Masqué, P., Duarte, C.M., 2018. Expanding Greenland seagrass meadows contribute new sediment carbon sinks. *Sci. Rep.* 8, 14024. <https://doi.org/10.1038/s41598-018-32249-w>.
- Montandon, L.M., Small, E.E., 2008. The impact of soil reflectance on the quantification of the green fraction from NDVI. *Remote Sens. Environ.* 112, 1835–1845. <https://doi.org/10.1016/j.rse.2007.09.007>.

- Mora-Soto, A., Palacios, M., Macaya, E., Gómez, I., Huovinen, P., et al., 2020. A high-resolution global map of giant kelp (*Macrocystis pyrifera*) forests and intertidal green algae (*Ulva* spp.) with Sentinel-2 imagery. *Remote Sens.* 12, 694. <https://doi.org/10.3390/rs12040694>.
- Morlighem, M., Williams, C.N., Rignot, E., An, L., Arndt, J.E., et al., 2017. BedMachine v3: complete bed topography and ocean bathymetry mapping of Greenland from multibeam echo sounding combined with mass conservation. *Geophys. Res. Lett.* 44, 11051–11061. <https://doi.org/10.1002/2017GL074954>.
- Mortensen, J., Bendtsen, J., Lennert, K., Rysgaard, S., 2014. Seasonal variability of the circulation system in a west Greenland tidewater outlet glacier fjord, Godthåbsfjord (64°N): Godthåbsfjord. *J. Geophys. Res.: Earth Surf.* 119, 2591–2603. <https://doi.org/10.1002/2014JF003267>.
- Mortensen, J., Lennert, K., Bendtsen, J., Rysgaard, S., 2011. Heat sources for glacial melt in a sub-Arctic fjord (Godthåbsfjord) in contact with the Greenland Ice Sheet. *J. Geophys. Res.* 116, C01013. <https://doi.org/10.1029/2010JC006528>.
- Mouginot, J., Rignot, E., Björk, A.A., van den Broeke, M., Millan, R., et al., 2019. Forty-six years of Greenland Ice Sheet mass balance from 1972 to 2018. *Proc. Natl. Acad. Sci.* 116, 9239–9244. <https://doi.org/10.1073/pnas.1904242116>.
- Moyer, A.N., Sutherland, D.A., Nienow, P.W., Sole, A.J., 2019. Seasonal variations in iceberg freshwater flux in Sermilik Fjord, Southeast Greenland from Sentinel-2 imagery. *Geophys. Res. Lett.* 46, 8903–8912. <https://doi.org/10.1029/2019GL082309>.
- Nechad, B., Ruddick, K.G., Park, Y., 2010. Calibration and validation of a generic multisensor algorithm for mapping of total suspended matter in turbid waters. *Remote Sens. Environ.* 114, 854–866. <https://doi.org/10.1016/j.rse.2009.11.022>.
- Nijland, W., Reshitnyk, L., Rubidge, E., 2019. Satellite remote sensing of canopy-forming kelp on a complex coastline: a novel procedure using the Landsat image archive. *Remote Sens. Environ.* 220, 41–50. <https://doi.org/10.1016/j.rse.2018.10.032>.
- Olesen, B., Krause-Jensen, D., Marbà, N., Christensen, P.B., 2015. Eelgrass *Zostera marina* in subarctic Greenland: dense meadows with slow biomass turnover in cold waters. *Mar. Ecol. Prog. Ser.* 518, 107–121. <https://doi.org/10.3354/meps11087>.
- O'Neill, J.D., Costa, M., 2013. Mapping eelgrass (*Zostera marina*) in the Gulf Islands National Park Reserve of Canada using high spatial resolution satellite and airborne imagery. *Remote Sens. Environ.* 133, 152–167. <https://doi.org/10.1016/j.rse.2013.02.010>.
- Ørberg, S.B., Krause-Jensen, D., Mouritsen, K.N., Olesen, B., Marbà, N., et al., 2018. Canopy-forming macroalgae facilitate recolonization of sub-Arctic intertidal fauna and reduce temperature extremes. *Front. Mar. Sci.* 5, 332. <https://doi.org/10.3389/fmars.2018.00332>.
- Over, J.-S., Ritchie, A.C., Kranenburg, C.J., Brown, J.A., Buscombe, D., et al., 2021. Processing Coastal Imagery With Agisoft Metashape Professional Edition, Version 1.6—Structure From Motion Workflow Documentation. United States Geological Survey Open File Report 2021-1039. <https://doi.org/10.3133/ofr20211039>.
- Pahlevan, N., Sarkar, S., Franz, B.A., Balasubramanian, S.V., He, J., 2017. Sentinel-2 Multi-Spectral instrument (MSI) data processing for aquatic science applications: demonstrations and validations. *Remote Sens. Environ.* 201, 47–56. <https://doi.org/10.1016/j.rse.2017.08.033>.
- Pottier, A., Catry, T., Trégarot, E., Maréchal, J.-P., Fayad, V., et al., 2021. Mapping coastal marine ecosystems of the National Park of Banc d'Arguin (PNBA) in Mauritania using Sentinel-2 imagery. *Int. J. Appl. Earth Obs. Geoinf.* 102, 102419. <https://doi.org/10.1016/j.jag.2021.102419>.
- Rantanen, M., Karpechko, A.Y., Lipponen, A., Nordling, K., Hyvärinen, O., et al., 2022. The Arctic has warmed nearly four times faster than the globe since 1979. *Commun. Earth Environ.* 3, 168. <https://doi.org/10.1038/s43247-022-00498-3>.
- Rezvanbehbahani, S., Stearns, L.A., Keramati, R., Shankar, S., van der Veen, C.J., 2020. Significant contribution of small icebergs to the freshwater budget in Greenland fjords. *Commun. Earth Environ.* 1, 31. <https://doi.org/10.1038/s43247-020-00032-3>.
- Richter, A., Rysgaard, S., Dietrich, R., Mortensen, J., Petersen, D., 2011. Coastal tides in West Greenland derived from tide gauge records. *Ocean Dyn.* 61, 39–49. <https://doi.org/10.1007/s10236-010-0341-z>.
- Rossiter, T., Furey, T., McCarthy, T., Stengel, D.B., 2019. Application of multiplatform, multi-spectral remote sensors for mapping intertidal macroalgae: a comparative approach. *Aquat. Conserv. Mar. Freshw. Ecosyst.* 30, 1595–1612. <https://doi.org/10.1002/aqc.3357>.
- Rouse, J., Haas, R., Schell, J., Deering, D., 1974. Monitoring Vegetation Systems in the Great Plains With ERTS. <https://doi.org/10.1002/mrm.26868> Washington, DC.
- Scheick, J., Enderlin, E.M., Hamilton, G.S., 2019. Semi-automated open water iceberg detection from Landsat applied to Disko Bay, West Greenland. *J. Glaciol.* 65, 468–480. <https://doi.org/10.1017/jog.2019.23>.
- Schild, K.M., Hawley, R.L., Chipman, J.W., Benn, D.L., 2017. Quantifying suspended sediment concentration in subglacial sediment plumes discharging from two Svalbard tidewater glaciers using Landsat-8 and in situ measurements. *Int. J. Remote Sens.* 38, 6865–6881. <https://doi.org/10.1080/01431161.2017.1365388>.
- Schoenrock, K., Vad, J., Muth, A., Pearce, D., Rea, B., Schofield, J., Kamenos, N., 2018. Biodiversity of kelp forests and coralline algae habitats in southwestern Greenland. *Diversity* 10, 117. <https://doi.org/10.3390/d10040117>.
- Schroeder, S.B., Dupont, C., Boyer, L., Juanes, F., Costa, M., 2019. Passive remote sensing technology for mapping bull kelp (*Nereocystis luetkeana*): a review of techniques and regional case study. *Glob. Ecol. Conserv.* 19, e00683. <https://doi.org/10.1016/j.gecco.2019.000683>.
- Sejr, M.K., Mouritsen, K.N., Krause-Jensen, D., Olesen, B., Blicher, M.E., Thyrring, J., 2021. Small scale factors modify impacts of temperature, ice scour and waves and drive rocky intertidal community structure in a Greenland Fjord. *Front. Mar. Sci.* 7, 607135. <https://doi.org/10.3389/fmars.2020.607135>.
- Smale, D.A., Burrows, M.T., Moore, P., O'Connor, N., Hawkins, S.J., 2013. Threats and knowledge gaps for ecosystem services provided by kelp forests: a northeast Atlantic perspective. *Ecol. Evol.* 3, 4016–4038. <https://doi.org/10.1002/ece3.774>.
- Sotille, M.E., Bremer, U.F., Vieira, G., Velho, L.F., Petsch, C., 2020. Evaluation of UAV and satellite-derived NDVI to map maritime Antarctic vegetation. *Appl. Geogr.* 125, 102322. <https://doi.org/10.1016/j.apgeog.2020.102322>.
- St-Pierre, A.P., Gagnon, P., 2020. Kelp-bed dynamics across scales: enhancing mapping capability with remote sensing and GIS. *J. Exp. Mar. Biol. Ecol.* 522, 151246. <https://doi.org/10.1016/j.jembe.2019.151246>.
- Straneo, F., Slater, D., Bouchard, C., Cape, M., Carey, M., Ciannelli, L., et al., 2022. An interdisciplinary perspective on Greenland's changing coastal margins. *Oceanography* <https://doi.org/10.5670/oceanog.2022.128>.
- Stuart-Lee, A.E., Mortensen, J., van der Kaaden, A.-S., Meire, L., 2021. Seasonal hydrography of ameralik: a Southwest Greenland Fjord impacted by a land-terminating glacier. *J. Geophys. Res. Oceans* 126, e2021JC017552. <https://doi.org/10.1029/2021JC017552>.
- Sulak, D.J., Sutherland, D.A., Enderlin, E.M., Stearns, L.A., Hamilton, G.S., 2017. Iceberg properties and distributions in three Greenlandic fjords using satellite imagery. *Ann. Glaciol.* 58, 92–106. <https://doi.org/10.1017/aog.2017.5>.
- Taddia, Y., Russo, P., Lovo, S., Pellegrini, A., 2020. Multispectral UAV monitoring of submerged seaweed in shallow water. *Appl. Geomatics* 12, 19–34. <https://doi.org/10.1007/s12518-019-00270-x>.
- Tejner, P., 2017. Indigenous modes of ownership: reopening the case for communal rights in Greenland. In: Peladeix, C., Basse, E.M. (Eds.), *Governance of Arctic Offshore Oil and Gas. Global Governance: A Review of Multilateralism and International Organizations*, Routledge, London, pp. 203–218.
- Thyrring, J., Wegeberg, S., Blicher, M.E., Krause-Jensen, D., Høglund, S., et al., 2021. Latitudinal patterns in intertidal ecosystem structure in West Greenland suggest resilience to climate change. *Ecography* 44, 1156–1168. <https://doi.org/10.1111/ecog.05381>.
- Vanhellemont, Q., 2019. Adaptation of the dark spectrum fitting atmospheric correction for aquatic applications of the Landsat and Sentinel-2 archives. *Remote Sens. Environ.* 225, 175–192. <https://doi.org/10.1016/j.rse.2019.03.010>.
- Wagner, T.J.W., Wadhams, P., Bates, R., Elsegui, P., Stern, A., et al., 2014. The “footloose” mechanism: Iceberg decay from hydrostatic stresses. *Geophys. Res. Lett.* 41, 5522–5529. <https://doi.org/10.1002/2014GL060832>.
- Wang, M., Hu, C., Barnes, B.B., Mitchum, G., Lapointe, B., et al., 2019. The great Atlantic Sargassum belt. *Science* 365, 83–87. <https://doi.org/10.1126/science.aaw7912>.
- Wessel, B., Huber, M., Wohlfart, C., Marschall, U., Kosmann, D., Roth, A., 2018. Accuracy assessment of the global TanDEM-X digital elevation model with GPS data. *ISPRS J. Photogramm. Remote Sens.* 139, 171–182. <https://doi.org/10.1016/j.isprsjprs.2018.02.017>.
- Wilson, K.L., Wong, M.C., Devred, E., 2020. Branching algorithm to identify bottom habitat in the optically complex coastal waters of Atlantic Canada using Sentinel-2 satellite imagery. *Front. Environ. Sci.* 8, 579856. <https://doi.org/10.3389/fenvs.2020.579856>.
- Wood, M., Rignot, E., Fenty, I., Menemenlis, D., Millan, R., et al., 2018. Ocean-induced melt triggers glacier retreat in Northwest Greenland. *Geophys. Res. Lett.* 45, 8334–8342. <https://doi.org/10.1029/2018GL078024>.
- Xiao, Y., Zhang, J., Cui, T., Gong, J., Liu, R., et al., 2019. Remote sensing estimation of the biomass of floating *Ulva prolifera* and analysis of the main factors driving the interannual variability of the biomass in the Yellow Sea. *Mar. Pollut. Bull.* 140, 330–340. <https://doi.org/10.1016/j.marpolbul.2019.01.037>.
- Zoffoli, M.L., Gernez, P., Rosa, P., Le Bris, A., Brando, V.E., et al., 2020. Sentinel-2 remote sensing of *Zostera noltei*-dominated intertidal seagrass meadows. *Remote Sens. Environ.* 251, 112020. <https://doi.org/10.1016/j.rse.2020.112020>.